Astronomy & Astrophysics manuscript no. Bethermin˙model
February 1, 2011

Modeling the evolution of infrared galaxies: A Parametric backwards evolution model

M. Béthermin[1,2], H. Dole[1,2], G. Lagache[1,2], D. Le Borgne[3], and A. Penin[1,2]

[1] Univ Paris-Sud, Laboratoire IAS, UMR8617, Orsay, F-91405
e-mail: matthieu.bethermin@ias.u-psud.fr
[2] CNRS, Orsay, F-91405
[3] Institut d'Astrophysique de Paris (IAP), UMR 7095 CNRS, UPMC, 98 bis boulevard Arago, F-75014 Paris, France

Submitted 30 September 2010 / Accepted 21 January 2011

Abstract

Aims. We aim at modeling the infrared galaxy evolution in a way as simple as possible and reproduce statistical properties among which the number counts between 15 μm and 1.1 mm, the luminosity functions, and the redshift distributions. We then aim at using this model to interpret the recent observations (*Spitzer*, Akari, BLAST, LABOCA, AzTEC, SPT and *Herschel*), and make predictions for *Planck* and future experiments like CCAT or SPICA.
Methods. This model uses an evolution in density and luminosity of the luminosity function parametrized by broken power-laws with two breaks at redshift ∼0.9 and 2, and contains the two populations of the Lagache et al. (2004) model: normal and starburst galaxies. We also take into account the effect of the strong lensing of high-redshift sub-millimeter galaxies. This effect is significant in the sub-mm and mm range near 50 mJy. It has 13 free parameters and 8 additional calibration parameters. We fit the parameters to the IRAS, *Spitzer*, *Herschel* and *AzTEC* measurements with a Monte-Carlo Markov chain.
Results. The model ajusted on deep counts at key wavelengths reproduces the counts from the mid-infrared to the millimeter wavelengths, as well as the mid-infrared luminosity functions. We discuss the contribution to the cosmic infrared background (CIB) and to the infrared luminosity density of the different populations. We also estimate the effect of the lensing on the number counts, and discuss the recent discovery by the South Pole Telescope (SPT) of a very bright population lying at high-redshift. We predict the contribution of the lensed sources to the *Planck* number counts, the confusion level for future missions using a P(D) formalism, and the Universe opacity to TeV photons due to the CIB. Material of the model (software, tables and predictions) is available at http://www.ias.u-psud.fr/irgalaxies/.

Key words. Cosmology: diffuse radiation - Galaxies: statistics - Galaxies: evolution - Galaxies: star formation - Infrared: galaxies - Submillimeter: galaxies

1. Introduction

The extragalactic background light (EBL) is the relic emission due to galaxy formation and accretion processes since the recombination. The infrared ($8\ \mu m < \lambda < 1000\ \mu m$) part of this emission called cosmic infrared background (CIB) was detected for the first time by Puget et al. (1996) and contains about half of the energy of the EBL (Dole et al. 2006; Béthermin et al. 2010a). Nevertheless, in the local universe, the optical/UV emissions are 3 times larger than infrared/sub-millimeter ones (Soifer & Neugebauer 1991; Driver et al. 2008). This pseudo-paradox is explained by a strong evolution of the properties of the infrared galaxies.

The infrared luminosity density is dominated by normal galaxies ($L_{IR,bolometric} < 10^{11} L_{\odot}$) in the local Universe (Saunders et al. 1990). At higher redshift, it is dominated by luminous infrared galaxies (LIRG, $10^{11} L_{\odot} < L_{IR,bolometric} < 10^{12} L_{\odot}$) at z=1 (Le Floc'h et al. 2005) and by ultra-luminous infrared galaxies (ULIRG, $10^{12} L_{\odot} < L_{IR,bolometric} < 10^{13} L_{\odot}$) at z=2 (Caputi et al. 2007). The infrared luminosity of these galaxies is correlated to the star formation rate (Kennicutt 1998). Thus modeling this rapid evolution of the infrared galaxies is very important to understand the history of the star formation.

The physical models (such as Lacey et al. (2010); Wilman et al. (2010); Younger & Hopkins (2010) for the latest) use a physical approach based on semi-analytical recipes and dark matter numerical simulations. They use a limited set of physical parameters, but they nowadays poorly reproduce some basic observational constraints like the infrared galaxy number counts (Oliver et al. 2010).

The backwards evolution models (like Lagache et al. (2004); Franceschini et al. (2010); Rowan-Robinson (2009); Valiante et al. (2009)) use an evolution the luminosity function (LF) of the galaxies to reproduce empirically the galaxy counts, and other constraints. These models make only a description of the evolution and contain little physics. The parameters of these models were tuned manually to fit observational constraints. Le Borgne et al. (2009) used an other approach and performed a non-parametric inversion of the counts to determine the LF. Nevertheless, this approach is complex, uses only one population of galaxy, and does not manage to reproduce the 160 μm number counts. An other fully-empirical approach was used by Dominguez et al. (2010). They fitted the SED from UV to mid-infrared of detected galaxies and extrapolated the far-infrared spectral energy distribution of these galaxies and the contribution of faint populations. Nevertheless, their model aims only to reproduce the CIB; however its ability to reproduce

other constraints like the number counts was not tested.

The Balloon-borne Large-Aperture Submillimeter Telescope (BLAST) experiment (Pascale et al. 2008; Devlin et al. 2009) and the spectral and photometric imaging receiver (SPIRE) instrument (Griffin 2010) onboard the *Herchel* space telescope (Pilbratt & al. 2010) performed recently new observations in the sub-mm at 250, 350 and 500 μm. In their current version, most of the models fail to reproduce the number counts measured at these wavelengths (Patanchon et al. 2009; Béthermin et al. 2010b; Clements et al. 2010; Oliver et al. 2010). The Valiante et al. (2009) model gives the best results, using a Monte Carlo approach (sources are randomly taken in libraries) to simulate the temperature scatter and the heterogeneity of the populations of active galactic nucleus (AGN), but this model strongly disagrees with the recent measurements of the redshift distribution of the CIB by Jauzac et al. (2010). It is thus necessary to develop new models that reproduce the recent far-infrared and sub-mm observations.

The discovery of very bright and high-redshift dusty galaxies by Vieira et al. (2009) with the south pole telescope (SPT) suggests that the contribution of high-redshift galaxies strongly lensed by dark matter halos of massive low-redshift galaxies on the bright sub-millimeter and millimeter counts is non negligible. This contribution was discussed by Negrello et al. (2007) and an observational evidence of this phenomenon was found very recently by Negrello et al. (2010). We can also cite the simplified approach of Lima et al. (2010) who reproduce the AzTEC and SPT counts using a single population of galaxies with a Schechter LF at a single redshift and a lensing model. We can also cite the very recent work of Hezaveh & Holder (2010) on the effect of the lensing on the SPT counts, based on an advanced lensing model.

We present a new simple and parametric model based on Lagache et al. (2004) SED libraries, which reproduces the new observational constraints. The parameters of this model (13 free parameters and 8 calibration parameters) were fitted from a large set of recent observations using a Monte-Carlo Markov chain (MCMC) method, allowing to study degeneracies between the parameters. This model also includes the effects of the strong lensing on the observations. We make predictions on the confusion limit for future missions, on the high-energy opacity of the Universe and on the effects of the strong lensing on the counts. This model is plugged to a halo model to study the spatial distribution of the infrared galaxies in a companion paper (Penin et al. 2010). Note that an other study using also MCMC methods was performed by Marsden et al. (2010) at the same time than ours.

We use the WMAP 7 year best-fit ΛCDM cosmology in this paper (Larson et al. 2010). We thus have $H_0 = 71$ km.s^{-1}.Mpc^{-1}, $\Omega_\Lambda = 0.734$ and $\Omega_m = 0.266$.

2. Approach

The backward evolution models are not built on physical parameters. Each model uses different evolving populations to reproduce the observational constraints. Some recent models (like Franceschini et al. (2010); Rowan-Robinson (2009)) use 4 galaxy populations evolving separately to reproduce the observations. Valiante et al. (2009) take randomly galaxy SEDs on a very large library of templates and claim that the contribution of the AGNs and the dispersion of the dust temperature of the galaxies must be taken into account to reproduce the observational constraint. Our approach is to keep the model as simple as possible, but to use advanced methods to constrain its free parameters. This new parametric model can be used as an input for halo modeling or P(D) analysis for instance.

As it will be shown, we did not need AGN contribution and temperature dispersion to reproduce the current observational constraints. In fact, in the local Universe, the AGNs only dominate the ULIRG regime (Imanishi 2009). Alexander et al. (2005) estimate an AGN contribution of 8% for the submillimeter galaxies (SMG). Recently Fadda et al. (2010) showed that the proportion of AGN-dominated sources is rather small for LIRGs at z∼1 (5%) and ULIRGs around z∼2 (12%). Jauzac et al. (2010) showed that AGN contribution to the CIB is less than 10% at z<1.5. These category of luminosity dominates the infrared output at their redshift. The low contribution of AGN in these categories explains why the AGNs are not necessary to reproduce the mean statistical properties of the galaxies. Nevertheless, despite their small contribution to the infrared output, the AGNs play a central role in the physics of galaxies.

Our model takes into account the the strong-lensing of high redshift galaxies by dark matter halos of elliptical galaxies. According to the results of Sect. 7.3, the effect of the lensing on the counts we fitted is smaller than 10%. The model of lensing does not have free parameters. It is based on WMAP-7-years-best-fit cosmology and on some parameters taken at values given by the litterature. The lensing is thus not useful to reproduce the current observations, but is necessary to make predictions at bright fluxes (>100 mJy) in the sub-mm and mm range, where the effects of the lensing are large.

3. Description of the model

3.1. Basic formulas

The flux density S_ν at a frequency ν of a source lying at a redshift z is (Hogg 1999) is

$$S_\nu = \frac{(1+z)L_{(1+z)\nu}}{4\pi D_L^2(z)} \tag{1}$$

where z is the redshift, D_L is the luminosity distance of the source, and $L_{(1+z)\nu}$ is the luminosity at a frequency $(1+z)\nu$. The comoving volume corresponding to a redshift slice between z and z+dz and a unit solid angle is

$$\frac{dV}{dz} = D_H \frac{(1+z)^2 D_A^2}{\sqrt{\Omega_\Lambda + (1+z)^3\Omega_m}} \tag{2}$$

where D_H is the Hubble distance ($D_H = c/H_0$), D_A the angular distance to the redshift z. Ω_m and Ω_Λ are the normalized energy density of the matter and of the cosmological constant.

3.2. Bolometric luminosity function and its evolution

We assume that the luminosity function (LF) is a classical double exponential function (Saunders et al. 1990)

$$\Phi(L_{IR}) = \Phi^\star \times \Big(\frac{L_{IR}}{L^\star}\Big)^{1-\alpha} \times exp\Big[-\frac{1}{2\sigma^2} log_{10}^2 (1+\frac{L_{IR}}{L^\star})\Big] \tag{3}$$

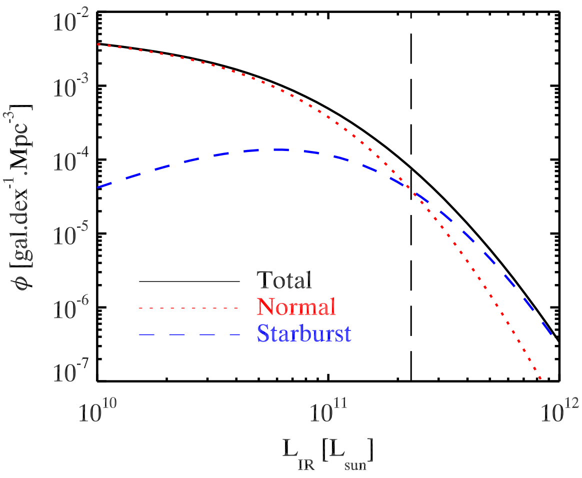

Figure 1. *Solid line*: Local infrared bolometric luminosity function from our best-fit model. *Red dotted line*: contribution of the normal galaxies. *Blue dashed line*: contribution of the starburst galaxies. *Black vertical long dashed line*: luminosity of the transition between the two population (L_{pop}).

where $\Phi(L_{IR})$ is the number of sources per logarithm of luminosity and per comoving volume unit for an infrared bolometric luminosity L_{IR}. $\Phi_\star$ is the normalization constant characterizing the density of sources. $L_\star$ is the characteristic luminosity at the break. $1-\alpha$ and $1-\alpha-1/\sigma^2/ln^2(10)$ are the slope of the asymptotic power-law behavior at respectively low and high luminosity.

We assume a continuous evolution in luminosity and in density of the luminosity function with the redshift of the form $L^\star \propto (1+z)^{r_L}$ and $\Phi^\star \propto (1+z)^{r_\Phi}$ where r_L and r_ϕ are coefficients driving the evolution in luminosity and density, respectively. It is impossible to reproduce the evolution of the LF with constant r_L and r_ϕ. We consequently authorize their value to change at some specific redshifts. The position of these breaks are the same for both r_L and r_ϕ. The position of the first redshift break is a free parameter and converge to the same final value for initial values between 0 and 2. To avoid a divergence at high redshift, we also add a second break fixed at z=2.

3.3. Spectral energy distribution (SED) of the galaxies

We use the Lagache et al. (2004) SED library. This library contains two populations: a starburst one and a normal one. This library is parametrized only by the infrared bolometric luminosity (L_{IR}). There is no evolution of the SED with the redshift. The normal population has a spectrum typical of spiral galaxy. The SED of this population does not evolve with L_{IR}. On the contrary, the starburst SED evolves with L_{IR}. The brighter the starburst galaxy, the hotter the dust.

The normal galaxies are dominant at low luminosity and the starburst at high luminosity. We thus chose arbitrary the following smooth function to describe the fraction of starburst galaxies as a function of the bolometric luminosity L_{IR}:

$$\frac{\Phi_{starburst}}{\Phi} = \frac{1 + th\Big[log_{10}(L_{IR}/L_{pop})/\sigma_{pop}\Big]}{2} \tag{4}$$

where th is the hyperbolic tangent function. L_{pop} is the luminosity at which the number of normal and starburst galaxies are equal. σ_{pop} characterizes the width of the transition between the two populations. At $L_{IR} = L_{pop}$, the fraction of starburst is 50%. There are 88% of starburst at $L_{IR} = L_{pop} \times 10^{\sigma_{pop}}$, and 12% at $L_{IR} = L_{pop} \times 10^{-\sigma_{pop}}$. The contribution of the different populations to the local infrared bolometric LF is shown in Fig. 1.

3.4. Observables

The number counts at different wavelengths are an essential constraint for our model. The source extraction biases are in general accurately corrected for these observables. The counts are computed with the following formula

$$\frac{dN}{dS_\nu d\Omega}(S_\nu) = \tag{5}$$

$$\sum_{pop} \int_0^\infty f_{pop}(L_{IR}) \frac{dN}{dL_{IR}dV}\Big|_{L_{IR}(S_\nu,z,pop)} \frac{dL_{IR}}{dS_\nu} \frac{dV}{dzd\Omega} dz \tag{6}$$

$$= \sum_{pop} \int_0^\infty \frac{dN}{dS_\nu dz d\Omega} dz \tag{7}$$

where $dN/dS_\nu/d\Omega$ is the number of source per flux unit and per solid angle. $f_{pop}(L_{IR})$ is the fraction of the sources of a given galaxy population computed with the Eq. 4. $dN/dL_{IR}/dV$ is computed from the Eq. 3

$$\frac{dN}{dL_{IR}dV} = \frac{dN}{dlog_{10}(L_{IR})L_{IR}log(10)dV} = \frac{\Phi(L_{IR})}{L_{IR}log(10)}. \tag{8}$$

$L_{IR}(S_\nu, z, pop)$ and dL_{IR}/dS_ν were computed on a grid in S_ν and z from the cosmology and the SED templates. These grids do not depend on the evolution of the LF nor on the population mixing parameters. These grids are thus generated only once and saved to accelerate the computation of the counts. Note that with this method, it is very easy to change the SED templates and/or add other populations.

Other measurements help to constraint our model. For example, the monochromatic luminosity Φ_{mono} function at a given redshift is

$$\Phi_{mono} = \sum_{pop} f_{pop}(L_{IR}(\nu L_\nu))\phi(L_{IR}(\nu L_\nu)) \frac{dlog_{10}(L_{IR})}{d(\nu L_\nu)}. \tag{9}$$

We do not use the bolometric LFs, because they are biased by the choice of the assumed SED of the sources.

We can also compute the redshift distribution N(z) for a selection in flux $S_\nu > S_{\nu,cut}$ with

$$N(z, S_{cut}) = \int_{S_{\nu,cut}}^\infty \frac{dN}{dS_\nu dz} dS_\nu. \tag{10}$$

The extragalactic background due to the galaxies at a given wavelength is

$$B_\nu = \int_{z=0}^\infty \int_{S_\nu=0}^\infty S_\nu \frac{dN}{dS_\nu dz d\Omega} dS_\nu\, dz = \int_{S_\nu=0}^\infty S_\nu \frac{dN}{dS_\nu d\Omega} dS_\nu \tag{11}$$

and can be compared to the measurements of the CIB.

Parameter	Description	Value
α	Faint-end slope of the infrared bolometric LF	1.223 ± 0.044
σ	Parameter driving the bright-end slope of the LF	0.406 ± 0.019
$L_\star$(z=0) ($\times 10^{10}$ $L_\odot$)	Local characteristic luminosity of the LF	2.377 ± 0.363
$\phi_\star$ (z=0) ($\times 10^{-3}$ gal/dex/Mpc^3)	Local characteristic density of the LF	3.234 ± 0.266
$r_{L_\star,lz}$	Evolution of the characteristic luminosity between 0 and $z_{break,1}$	2.931 ± 0.119
$r_{phi_\star,lz}$	Evolution of the characteristic density between 0 and $z_{break,1}$	0.774 ± 0.196
$z_{break,1}$	Redshift of the first break	0.879 ± 0.052
$r_{L_\star,mz}$	Evolution of the characteristic luminosity between $z_{break,1}$ and $z_{break,2}$	4.737 ± 0.301
$r_{phi_\star,mz}$	Evolution of the characteristic density of between $z_{break,1}$ and $z_{break,2}$	-6.246 ± 0.458
$z_{break,2}$	Redshift of the second break	2.000 (fixed)
$r_{L_\star,hz}$	Evolution of the characteristic luminosity for z> $z_{break,2}$	0.145 ± 0.460
$r_{phi_\star,hz}$	Evolution of the characteristic density for z> $z_{break,2}$	-0.919 ± 0.651
L_{pop} ($\times 10^{10}$ $L_\odot$)	Luminosity of the transition between normal and starburst templates	23.677 ± 2.704
σ_{pop}	Width of the transition between normal and starburst templates	0.572 ± 0.056

Table 1. Parameters of our model fitted to our selection of infrared observations. The errors are derived from the MCMC analysis.

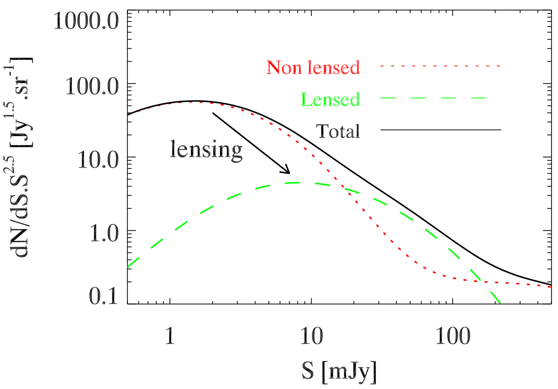

Figure 2. Effect of the lensing on the number counts at 850 microns. The contribution of lensed source is multiply by 10 to underline the effect of the lensing on the counts. *Red dotted line*: counts of non-lensed sources. *Green dashed line*: counts of lensed sources. *Black solid line*: total counts.

The level of the non-correlated fluctuations (shot-noise) of the CIB can be easily computed from our model with the equation:

$$P_{SN} = \int_0^{S_{\nu,cut}} S_\nu^2 \frac{dN}{dS_\nu d\Omega} dS_\nu \tag{12}$$

where P_{SN} is the level of the non-correlated fluctuations and $S_{\nu,cut}$ the flux limit for the cleaning of the resolved sources.

3.5. Effect of the strong lensing on the counts

We use a simple strong lensing model based on Perrotta et al. (2001, 2002). It supposes that the dark matter halos are singular isothermal spheres. The cross-section σ of a halo for a magnification μ larger than μ_{min} is

$$\sigma(\mu > \mu_{min}) = \frac{4\pi\alpha^2 D_{A,ls}}{\mu^2} \tag{13}$$

where $D_{A,ls}$ is the angular-diameter distance between the lens and the source and α is given by

$$\alpha = 4\pi \frac{\sigma_v^2}{c^2} \tag{14}$$

where c is the speed of light and σ_v the velocity dispersion in the halo, which depends on the cosmology, the redshift and the mass of the halo.

The probability $P(\mu_{min}, z_s)$ for a source at a redshift z_s to be magnified by a factor greater than μ_{min} is

$$P(\mu > \mu_{min}, z_s) = \tag{15}$$

$$\frac{(1+z_s)^2}{4\pi D_c(z_s)} \int_0^{z_s} \int_0^{\infty} \frac{dN}{d(log_{10}(M))\, dV} \sigma(\mu > \mu_{min}) \frac{dV}{dz} dM dz \tag{16}$$

where z_s is the redshift of the source, D_c the comoving radial distance, $\frac{dN}{d(log_{10}(M))\, dV}$ is the halo mass function, and $\frac{dV}{dz}$ is the comoving volume associated to the redshift slice dz. We use the halo mass function of Reed et al. (2007).

The counts derived by our model take into account the fact that a small fraction of the sources are gravitationally magnified. The observed number counts taking into account the lensing $(dN/dS_\nu/d\Omega)_{lensed}$ are computed from initial counts $dS_\nu/dz/d\Omega$ with

$$\left(\frac{dN}{dS_\nu d\Omega}\right)_{lensed}(S_\nu) = \tag{17}$$

$$\int_0^\infty \int_{\mu_{min}}^{\mu_{max}} \frac{dP}{d\mu}(z) \frac{1}{\mu} \frac{dN}{dS_\nu dz d\Omega} \left(\frac{S_\nu}{\mu}, z\right) d\mu\, dz. \tag{18}$$

Practically, this operation is performed multiplying the vector containing the counts for a given redshift slice by a matrix describing the effect of lensing. This lensing matrix has diagonal coefficients values around 1, and small ($< 10^{-3}$) non-diagonal terms. These non-diagonal terms describe how magnified faint sources affect the counts at brighter flux. The effect on the monochromatic luminosity function was computed in the same way. We chose $\mu_{min} = 2$ which corresponds to the limit of the validity of the strong-lensing hypothesis (Perrotta et al. 2001). The spatial extension of the lensed galaxies limits the maximum magnification. According to Perrotta et al. (2002), μ_{max} is in the 10-30 range. We chose to use μ_{max}=20 in this paper. Negrello et al. (2007) used μ_{min}=2 and μ_{max}=15.

Fig. 2 illustrates how number counts are affected by lensing. This figure is based on the number counts predicted by the model at 850 μm with a probability of magnification multiplied by a factor 10 to better show this effect. The green dashed line is contribution of the lensed sources. Due to the magnification, the peak of this contribution is at higher flux than for non-lensed

sources, and due to the small probability of lensing, the peak is lower than for non-lensed sources. This effect of the magnification on the counts become non negligible when the slope of the counts is very steep, like in the sub-mm and mm domain.

4. Fitting the model parameters on the data

Our model has several free parameters. We tried to have the minimum number of parameters. We determined them by fitting the model to published measurements of the counts and LFs. We used a Monte-Carlo Markov chain (MCMC) to find the best parameters, their uncertainties, and degeneracies. We do not fit the measured redshift distributions, because the cosmic variance and the selection effects are currently not enough accurately known.

4.1. Data: extragalactic number counts

4.1.1. Data used for the fit

We have chosen to fit the following data:

- *Spitzer* MIPS counts of Béthermin et al. (2010a) at 24, 70 and 160 μm,
- *Herschel* SPIRE Oliver et al. (2010) counts at 250, 350 and 500 μm,
- AzTEC counts of Austermann et al. (2010) and Scott et al. (2010) at 1.1 mm.

4.1.2. Justification of our choice

We fit only the differential number counts since the integral counts are highly correlated and the correlation matrix is rarely estimated.

The number counts were measured at numerous bands between 15 μm and 1.1 mm. We have chosen a collection of points. We were guided by the reliability of the measurements and their error bars.

Number counts at 15 μm based on the infrared space observatory (ISO) data (Elbaz et al. 1999; Gruppioni et al. 2002) and on the Akari data (Pearson et al. 2010; Hopwood et al. 2010) exhibit a discrepancy by a factor of about 2, and their errors do not include cosmic variance. The results of these papers were not fitted. Nevertheless, we compared a posteriori to our results to check consistency in Sect. 5.4.

We fitted the *Spitzer* MIPS counts of Béthermin et al. (2010a) at 24, 70 and 160 μm. These points were built from the data of FIDEL, COSMOS and SWIRE legacy programs. The errors bars take into account the cosmic variance. These counts agree with previous *Spitzer* measurements of Papovich et al. (2004); Shupe et al. (2008); Le Floc'h et al. (2009); Frayer et al. (2009) and *Herschel* measurements of Berta et al. (2010) (in which the different fields are not combined).

At 250 μm, 350 μm and 500 μm, we fitted *Herschel* SPIRE Oliver et al. (2010) counts which take into account the cosmic variance and the deboosting uncertainty. These counts agree with the BLAST measurements of Patanchon et al. (2009) and Béthermin et al. (2010b) and the *Herschel* measurements of Clements et al. (2010). We chosen Oliver et al. (2010) counts because *Herschel* data are better than BLAST ones and because Clements et al. (2010) counts use only Poissonian error bars, which could be largely underestimated. For instance, Béthermin et al. (2010a) estimate that the Poissonian uncertainties underestimate the real sample uncertainties by a factor 3 for counts around 100 mJy at 160 μm in a 10 deg^2 field.

We do not fit the 850 μm observation because of the large discrepancies between the submillimeter common-user bolometer array (SCUBA) observations (Coppin et al. 2006) and the large APEX bolometer Camera (LABOCA) ones (Weiß et al. 2009). We discuss this problem in the Sect. 5.4.

We fitted the AzTEC measurements at 1.1 mm of Austermann et al. (2010) and Scott et al. (2010). The area covered by AzTEC is small compared to *Spitzer* and *Herschel*. We used two independent measurements of the AzTEC counts to increase the weight of mm observations in our fit.

4.2. Data: monochromatic luminosity functions

4.2.1. Data used for the fit

We have chosen to fit the following data:

- IRAS local luminosity function at 60 μm of Saunders et al. (1990)
- *Spitzer* local luminosity function at 24 μm of Rodighiero et al. (2009),
- *Spitzer* luminosity function at 15 μm at z=0.6 of Rodighiero et al. (2009),
- *Spitzer* luminosity function at 12 μm at z=1 of Rodighiero et al. (2009),
- *Spitzer* luminosity function at 8 μm at z=2 of Caputi et al. (2007),

4.2.2. Justification of our choice

We fitted some monochromatic luminosity functions. We chose only wavelengths and redshifts for which no K-corrections are needed. These observations strongly constrain the parameters driving the redshift evolutions of our model.

From the Rodighiero et al. (2009) LFs measured with the *Spitzer* data at 24 μm, we computed 3 non K-corrected LFs at z=0, 0.6 and 1. We used their local LF at 24 μm. At z = 0.6 and 1, instead of using directly their results in their redshift bins, we combined their 15 μm LF at z=0.6 (respectively 12 μm LF at z=1) in the $0.45 < z < 0.6$ and $0.6 < z < 0.8$ bins (respectively $0.8 < z < 1.0$ and $1.0 < z < 1.4$) to obtain 15 μm LF at z=0.6 (respectively 12 μm LF at z=1). The error on a point is the maximum of the combination of the statistical errors of the two bins and of the difference between the measures in the two bins. The second value is often larger due to the quick evolution of the LF and the cosmic variance. We fitted only the points that do not suffer incompleteness to avoid possible biases. We also fitted the 8 μm at z=2 of Caputi et al. (2007).

We also fitted the local LF at 60 μm determined from the infrared astronomical satellite (IRAS) data (Saunders et al. 1990) to better constrain the faint-end slope of the local LF. Due to the strong AGN contamination at 60 μm in the ULIRG regime, we did not fit the points brighter than $10^{11.5}$ $L_\odot$ at 60 μm.

Instrument	Calibration parameter (γ_b)	Calib. uncertainty
MIPS 24 μm	1.00±0.03	4%
MIPS 70 μm	1.06±0.04	7%
MIPS 160 μm	0.96±0.03	12%
SPIRE 250 μm	0.88±0.05	15%
SPIRE 350 μm	0.97±0.07	15%
SPIRE 500 μm	1.17±0.1	15%
AzTEC 1.1 mm	0.98±0.09	9%

Table 2. Calibration parameters and 1-σ marginalized errors from our MCMC fit compared with calibration uncertainties given by the instrumental teams.

4.3. Data: CIB

The bulk of the CIB is not resolved at SPIRE wavelengths. We thus used the absolute measurement of the CIB level in SPIRE bands as a constraint for our model. We used the Lagache et al. (1999) measurement performed on the far-infrared absolute spectrophotometer (FIRAS) data: 11.7±2.9 nW.m^2.sr^{-1} at 250 μm, 6.4±1.6 nW.m^2.sr^{-1} at 350 μm and 2.7±0.7 nW.m^2.sr^{-1} at 500 μm. We assume that the CIB is only due to galaxies and thus neglect a possible extragalactic diffuse emission.

4.4. Calibration uncertainties

The calibration uncertainty is responsible for correlated uncertainties between points measured at a given wavelength with the same instrument. A change in the calibration modifies globally the number counts and the LF. Assuming the "good" calibration is obtained in multiplying the fluxes by a factor γ, the "good" normalized counts are obtained with $S_{new} = \gamma S$ and $(S_{good}^{2.5} dN/dS_{good}) = \gamma^{1.5}(S^{2.5}dN/dS)$. The effect on the LF in dex per volume unit is more simple. We just have to shift the luminosity in abscissa by a factor γ.

We added to our free parameters a calibration parameter for each fitted band (see Table 2). We took into account the uncertainties on the calibration estimated by the instrumental team in our fit (Stansberry et al. 2007; Gordon et al. 2007; Engelbracht et al. 2007; Swinyard et al. 2010; Scott et al. 2010).

4.5. Fitting method

To fit our points, we assumed that the uncertainties on the measurements and on the calibrations are Gaussian and not correlated. The log-likelihood is then

$$-\,log(L(\theta)) = \sum_{k=1}^{Npoints} \frac{(m_k - m_{model,k}(\theta))^2}{2\sigma_m^2} + \sum_{b=1}^{Nband} \frac{(\gamma_b - 1)^2}{2\sigma_{calib,b}^2} \quad (19)$$

where L is the likelihood, θ the parameters of the model, m_k a measurement, $m_{model,k}$ the prediction of the model for the same measurement, σ_m the measurement uncertainty on it, γ_b the calibration parameter of the band b and $\sigma_{calib,b}$ the calibration uncertainty for this band.

We used a Monte Carlo Markov chain (MCMC) Metropolis-Hastings algorithm (Chib & Greenberg 1995; Dunkley et al. 2005) to fit our model. The method consists in a random walk in the parameter space. At each step, a random shift of the parameters is done using a given fixed proposal density. A step n is kept with a probability of 1 if $L(\theta_n) > L(\theta_{n-1})$ or with a probability $L(\theta_n)/L(\theta_{n-1})$ else. The distribution of the realization of the chain is asymptotically the same as the underlying probability density. This property is thus very convenient to determine the confidence area for the parameters of the model.

We used the Fisher matrix formalism to determine the proposal density of the chain from initial parameters values set manually. The associated Fisher matrix is:

$$F_{ij}(\theta) = \sum_{k=1}^{Npoints} \frac{\partial m_{model,k}}{\partial \theta_i} \frac{\partial m_{model,k}}{\partial \theta_j} \frac{1}{2\sigma_m^2} \left(+ \frac{1}{2\sigma_{calib,b}^2} \right) \quad (20)$$

where θ is a vector containing the model and calibration (γ_b) parameters. The term in brackets appears only for the diagonal terms corresponding to a calibration parameter. We ran a first short chain (10 000 steps) and computed a new proposal density with the covariance matrix of the results. We then ran a second long chain of 300 000 steps. The final chain satisfies the Dunkley et al. (2005) criteria ($j^\star > 20$ and $r < 0.01$).

5. Results of the fit

5.1. Quality of the fit

Our final best-fit model have a χ^2 ($\chi^2 = -2log(L)$ because all errors are assumed to be Gaussian) of 177 for 113 degrees of freedom. Our fit is thus reasonably good. The parameters found with the fit are given in Table 1 (the uncertainties are computed from the MCMC). The calibration factor are compatible with the calibration uncertainties given by the instrumental teams with a χ^2 of 2.89 for 7 points (see Table 2). The results are plotted in Fig. 3.

5.2. Comparison between the model and the observed counts used in the fit

The Béthermin et al. (2010a) points fit globally well, with some exceptions. Our model is lower by about 15% than two points around 300 μJy at 24 μm. These two points are built combining the FIDEL, COSMOS and SWIRE fields. The SWIRE fields are shallow fields and the counts could be affected by the Eddington bias. We also observe a slight under-prediction of the bright (S_{70} >50 mJy) counts at 70 μm. We also plotted the Berta et al. (2010) counts at 160 μm measured using the photodetector array camera and spectrometer (PACS) on the *Herschel* satellite. These counts agree with Béthermin et al. (2010a) and our model.

Our model fits globally well the Oliver et al. (2010) and Béthermin et al. (2010b) counts, excepting a slight under-prediction of the counts between 30 mJy and 100 mJy at 500 μm. There is a mild disagreement with the Clements et al. (2010) counts, but their errors bars do not take into account the cosmic variance and are thus underestimated. We also plotted the results of the P(D) analysis of Glenn et al. (2010). These points and especially the error bars must be interpreted with caution (see the complete discussion in Glenn et al. (2010)). We have plotted the knots of the smooth and power-law models. They globally agree with our model.

Our model agrees very well with the AzTEC counts of Austermann et al. (2010) and Scott et al. (2010). The contribution of the strong lensing objects to the AzTEC counts is weak (<10%, see Sect. 7.3).

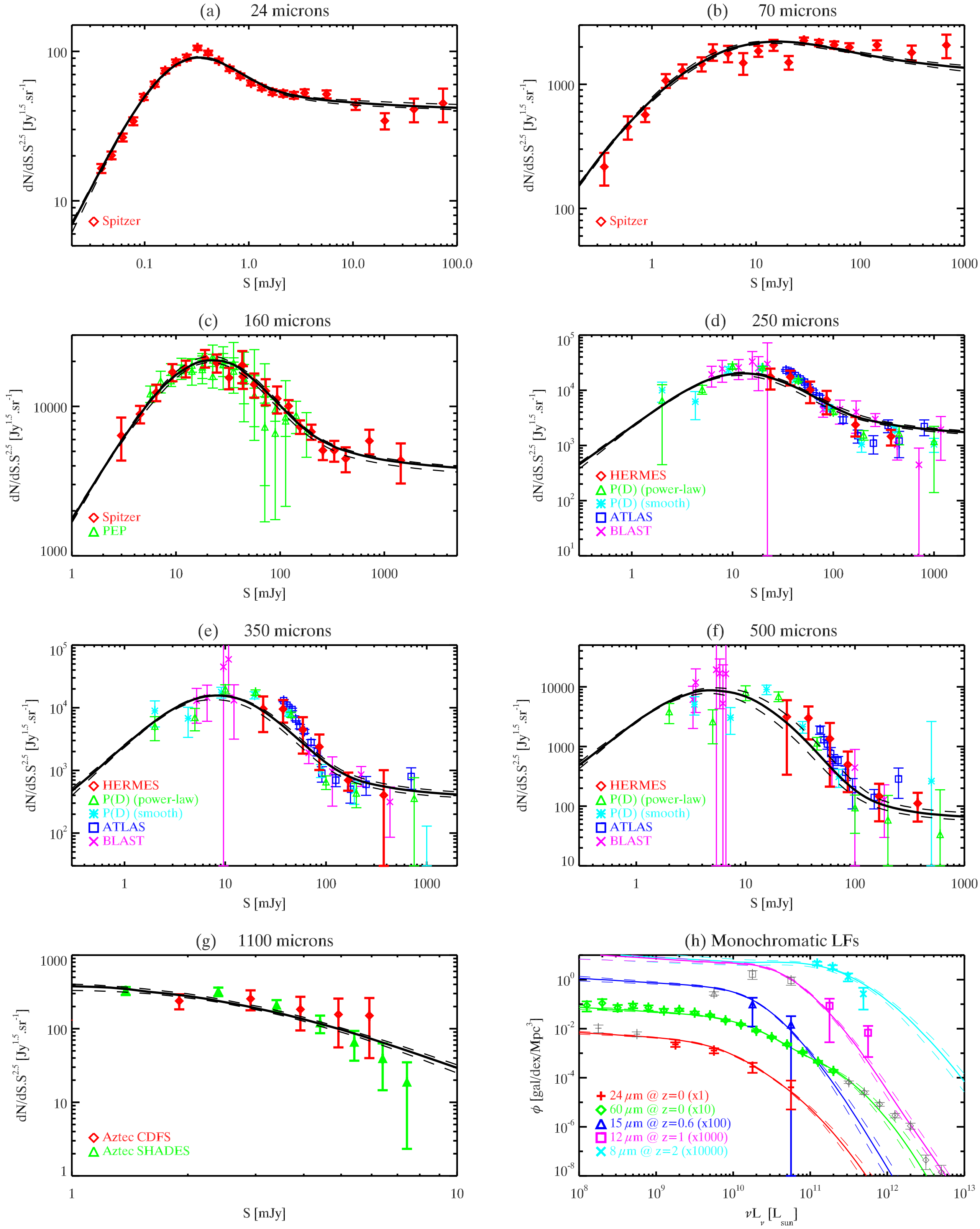

Figure 3. (a) to (f): Differential extragalactic number counts used for the fit. (h): Monochromatic LFs at different wavelengths and redshifts. (a) to (h): The fitted points are thicker. *Black solid line*: our best-fit model. *Black dashed line*: 1-σ range of the model. (a) to (c): *Red diamonds*: Béthermin et al. (2010a) *Spitzer* legacy number counts. (c): *Green triangles*: Berta et al. (2010) *Herschel*/PEP number counts. (d) to (f): *Red diamonds*: Oliver et al. (2010) *Herschel*/Hermes number counts. *Green triangles*: Glenn et al. (2010) *Herschel*/Hermes P(D) analysis. Clements et al. (2010) *Herschel*/ATLAS number counts. *Purple cross*: Béthermin et al. (2010b) BLAST number counts. (g): *Green triangles*: Scott et al. (2010) AzTEC number counts in the CDFS field. *Green triangles*: Austermann et al. (2010) AzTEC number counts in the SHADES field. (h): *Red plus*: Rodighiero et al. (2009) local 24 μm LF (not fitted points in grey). *Green diamonds*: Saunders et al. (1990) local 60 μm LF (shifted by a factor 10 on the y-axis; not fitted points in grey); *Blue triangles*: Rodighiero et al. (2009) 15 μm LF at z=0.6 (shifted by a factor 100 on the y-axis; not fitted points in grey). *Purple squares*: Rodighiero et al. (2009) 12 μm LF at z=1 (shifted by a factor 1000 on the y-axis; not fitted points in grey). *Cyan crosses*: Caputi et al. (2007) 8 μm LF at z=2 (shifted by a factor 10 000 on the y-axis).

5.3. Comparison between the model and the observed monochromatic LFs

Our model fits well our collection of LFs (Saunders et al. 1990; Caputi et al. 2007; Rodighiero et al. 2009), excepting the brightest point of Caputi et al. (2007). In Fig. 3, we arbitrary shifted the different LFs on the y-axis to obtain a clearer plot. Our model underestimates the 60 μm local LF in the ULIRG regime. It is expected because our model do not contain AGNs and confirms our choice of not fitting these points (Sect. 4.2).

5.4. Comparison between the model and the observed counts not used in the fit

We also compared our results with the counts at other wavelengths. They are plotted on Fig. 4 and 5. The 1-σ region of the model includes the γ_b uncertainty of Akari at 15 μm (4%, Ishihara et al. (2010)), PACS at 110 μm (about 10%, Berta et al. (2010)) and LABOCA at 850 μm (8.5%, Weiß et al. (2009)). The uncertainty on γ_b is about the same for LABOCA and SCUBA (~10%, Scott et al. (2006)). The uncertainties on the model are larger at these non-fitted wavelengths because the correlations between the model and the calibration parameters are not taken into account by the fit.

At 15 μm, the Elbaz et al. (1999) counts from different fields are not compatible between them, but our counts pass in the cloud of points. The Gruppioni et al. (2002) counts are significantly lower than our model and other works. We marginally agree with the Pearson et al. (2010) counts. The Hopwood et al. (2010) counts measured with Akari in a field around Abell 2218 are lower than our model by about 25%. Nevertheless, their field is very narrow and their estimation may suffer from cosmic variance. Finally, we well agree with the very recent Teplitz et al. (2010) measurements performed with the infrared spectrograph (IRS) onboard the *Spitzer* space telescope.

We compare our counts to Hacking & Houck (1987), Lonsdale et al. (1990), Rowan-Robinson et al. (1990), Saunders et al. (1990), Gregorich et al. (1995) and Bertin et al. (1997) at 60 μm from IRAS data. There are disagreements between the different observations and some error bars may be underestimated, but our model globally agrees with the cloud of points.

We can also compare the prediction of our model with Berta et al. (2010) counts at 110 μm. Our model globally agrees with their work. Nevertheless, our model tends to be higher than their measurement near 100 mJy. Observations on several larger fields will help to see if this effect is an artifact or not.

At 850 μm, we very well agree with the P(D) analysis of the LABOCA data of Weiß et al. (2009) (see Fig. 5). But, the measurements performed with SCUBA (Borys et al. 2003; Scott et al. 2006; Coppin et al. 2006) and LABOCA (Beelen et al. 2008) are significantly higher than our model at 6 and 8 mJy. At low flux (<2 mJy), our model agrees very well with the measurement performed in lensed region (Smail et al. 2002; Knudsen et al. 2008; Zemcov et al. 2010).

We also compare our model predictions with SPT measurements at 1.38 mm (Vieira et al. 2009). At this wavelength, the contribution of the synchrotron emission of the local radio-galaxies to the counts is not negligible. Nevertheless, these sources can be separated from dusty galaxies considering their spectrum. We thus compare our results with the counts of dusty sources. Vieira et al. (2009) measured counts for all the dusty sources and for the dusty sources without IRAS 60 μm counterpart. Our model agrees with these two measurements. Fig. 6 shows the counts of the non-IRAS dusty sources. The 7.2% cali-

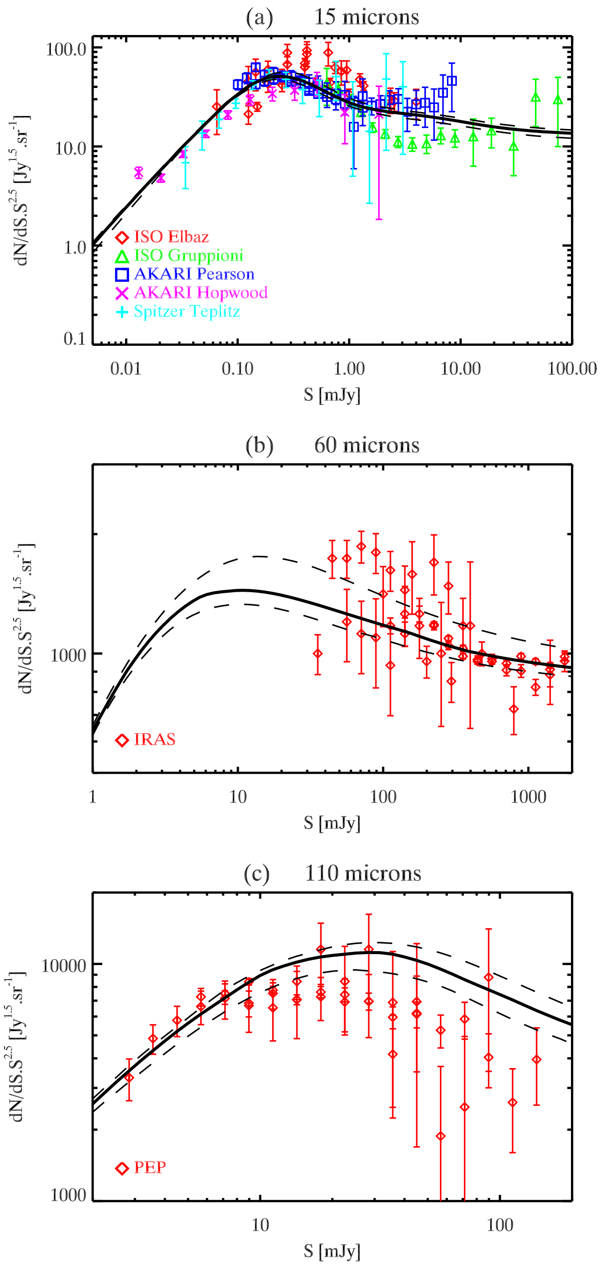

Figure 4. (a) to (c): Differential extragalactic number counts not used for the fit. *Black solid line*: our best-fit model. *Black dashed line*: 1-σ range of the model. (a): *Red diamonds*: Elbaz et al. (1999) ISO counts. *Green triangle*: Gruppioni et al. (2002) ISO counts. *Blue squares*: Pearson et al. (2010) Akari counts. *Purple cross*: Hopwood et al. (2010) Akari (lensed) counts. *Cyan plus*: Teplitz et al. (2010) *Spitzer*/IRS counts. (b): *Red diamonds*: Hacking & Houck (1987), Lonsdale et al. (1990), Rowan-Robinson et al. (1990), Saunders et al. (1990), Gregorich et al. (1995) and Bertin et al. (1997) IRAS counts. (c): *Red diamonds*: Berta et al. (2010) *Herschel*/PEP counts.

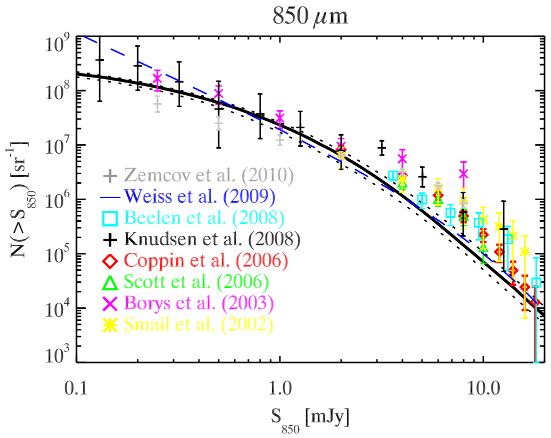

Figure 5. Integral number counts at 850 μm. *Black solid line*: our best-fit model. *Black dashed line*: 1-σ range of the model. *Grey plus*: Zemcov et al. (2010) combined SCUBA lensed counts. *Blue dashed line*: Weiß et al. (2009) LABOCA P(D) (Schechter model). *Red diamonds*: Coppin et al. (2006) SCUBA SHADES counts. *Cyan square*: (Beelen et al. 2008) LABOCA counts around the J2142-4423 Lyα protocluster. *Black plus*: Knudsen et al. (2008) combined SCUBA lensed counts; *Green triangles*: Scott et al. (2006) revisited SCUBA counts. *Purple cross*: Borys et al. (2003) SCUBA HDFN counts. *Yellow asterisks*: Smail et al. (2002) lensed counts.

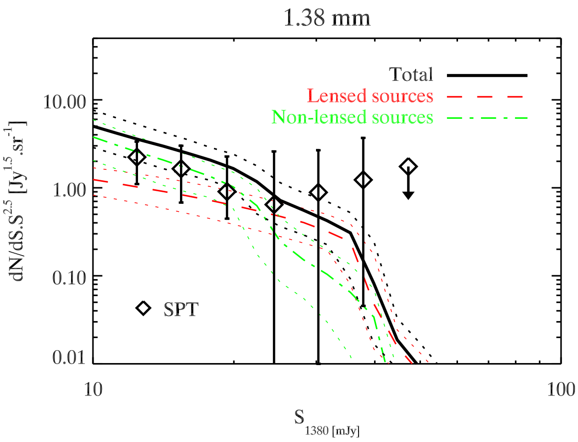

Figure 6. Number counts at 1.38 mm of dusty sources without IRAS 60 μm counterpart . *Black diamonds*: Vieira et al. (2009) south pole telescope (SPT) measurements. *Black solid line*: Total contribution of $S_{60} < 0.2$ Jy sources. *Green dot-dashed line*: Contribution of the non-lensed sources. *Red dashed line*: Contribution of the strongly-lensed sources. *Dotted lines* 1-σ contours.

bration uncertainty of SPT is taken into account in the 1-σ region of the model.

5.5. Comparison with the observed redshift distributions

In Fig. 7, we compare our model predictions with observed redshift distributions. At 24 μm, our model over-predicts by about 20% the number of sources below z=1 compared to Le Floc'h et al. (2009) observations for the selection $S_{24} > 80\mu$Jy. Nevertheless, they exclude i^{+}_{AB}<20 galaxies and their number of sources at low redshift is thus underestimated.

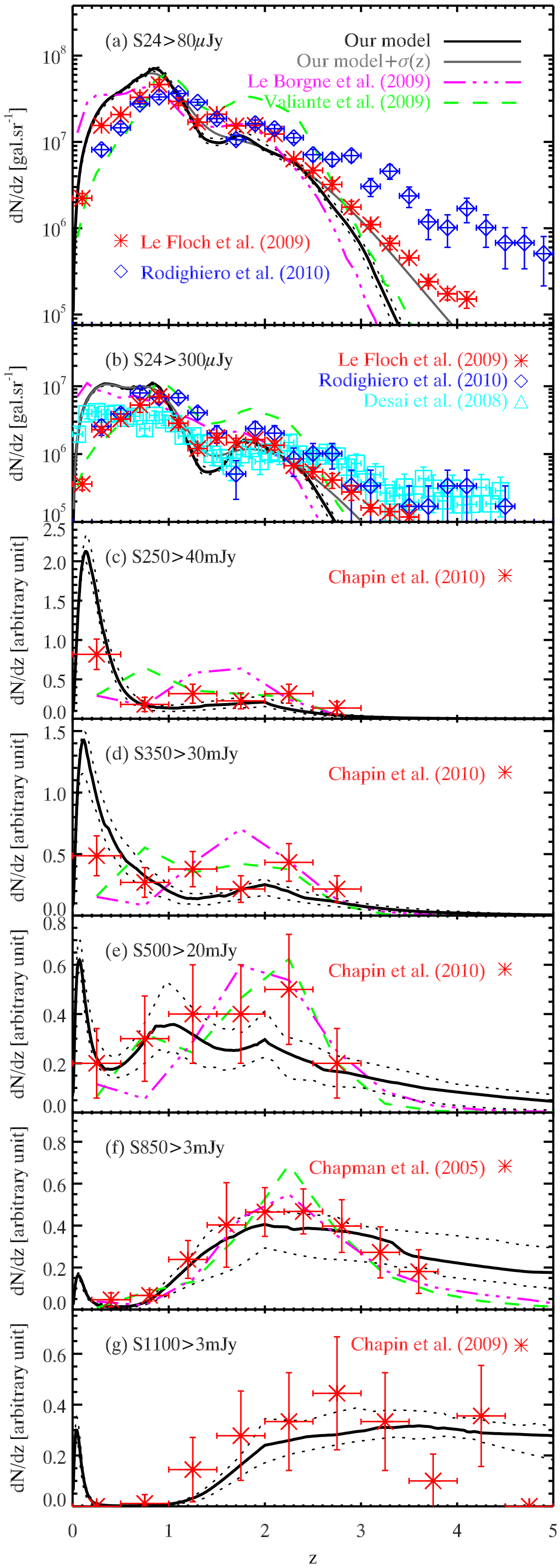

Figure 7. Redshift distribution of the S_{24} >80 μJy (a), S_{24} >300 μJy (b), S_{250} >40 mJy (c), S_{350} >30 mJy (d), S_{500} >20 mJy (e), S_{850} >3 mJy (f), S_{1100} >3 mJy (g) sources. These measurements are not fitted. *Black solid line*: our best-fit model. *Black dotted line*: 1-σ range of the model. *Grey solid line*: our best-fit model convolved by a gaussian of $\sigma_z = 0.125z$. *Purple three dot-dashed line*: Le Borgne et al. (2009) model. *Green dashed line*: Valiante et al. (2009) model. *Red asterisks*: Le Floc'h et al. (2009) (a, b), Chapin et al. (2010) (c, d, e), Chapman et al. (2005) (f) and Chapin et al. (2009) (g) measurements. *Blue diamonds*: Rodighiero et al. (2009) measurements(a, b). *Cyan squares*: Desai et al. (2008) measurements (b).

Our model also underpredicts the number of sources at z>3. But, the redshifts of the z>2 sources are only moderately accurate ($\sigma_z \approx 0.25$ for i^+_{AB} >25 at z∼2). Because of the strong slope of the redshift distribution, a significant number of sources measured near z=3.5 could be sources lying around z=3 with overestimated redshift. If we convolve our model with a gaussian error with $\sigma_z = 0.125z$ to simulate the redshift uncertainties, the model and the measurements agrees (Fig. 7). The Le Borgne et al. (2009) model agrees very well with the measurements, excepting at z<0.5 and z>2.5. The Valiante et al. (2009) model poorly reproduces this observation. The same observables was measured by Rodighiero et al. (2009). Their results are in agreement with Le Floc'h et al. (2009), excepting at z>3, where they are higher. It could be explain by a larger σ_z at high redshift.

We also compare the model with the redshift distribution of $S_{24} > 300\mu$Jy sources measured by Le Floc'h et al. (2009), Rodighiero et al. (2009) and Desai et al. (2008). These different measurements exhibit disagreements below z=0.5. This difference could be explained by the removing of the brightest optical sources (see previous paragraph). Our model overestimates the number of sources at z<0.5 by a factor 2. There is a rather good agreements between the models and the measurements between z=0.5 and z=2.5, except a small overestimation by Valiante et al. (2009) near z=2. At higher redshifts, the measurements are significantly higher than the models. It could be explained by two reasons: an effect of the redshift uncertainties and the absence of AGN in our model.

We compare with the Chapin et al. (2010) redshift distributions of the BLAST isolated sources at 250 μm, 350 μm and 500 μm. This selection of isolated sources does not allow to know the effective size of the field. We thus normalized our model and the measured counts to have $\int dN/dzdz = 1$. Our predicted redshift distribution globally fits the measurements, except at low z at 250 μm and 350 μm. This difference could be explained by the selection of isolated sources, which could miss sources in structures at low redshift. The other models (Le Borgne et al. 2009; Valiante et al. 2009) underpredicts the number of sources at low z. Valiante et al. (2009) also slightly overpredicts the number of sources at z∼1.5.

We compared the redshift distribution of the SCUBA sources at 850 μm with the prediction of our model. We use the selection-corrected measurements of Chapman et al. (2005) used by Marsden et al. (2010). All the models agrees with this measurement.

We also compared the prediction of our model with the redshift distribution of the sources detected at 1.1 mm by AzTEC (Chapin et al. 2009). A significant part of the sources detected at this wavelength (10 over 28) are not identified, and the selection is not performed in flux, but in signal-to-noise ratio. Consequently, the normalization of the redshift distribution is not known. We thus use the same normalization than for the BLAST redshift distributions ($\int dN/dzdz = 1$). The behavior predicted by our model agrees well with the observations.

Recently, Jauzac et al. (2010) has measured the contribution of the $S_{24} > 80$ μJy to the CIB at 70 and 160 μm as a function of the redshift. Their stacking analysis allows to check the total far-infrared (FIR) emissions of the faint sources not resolved at these wavelengths. Our model agrees well with their results, except near z=0.5 (see Fig. 8), where their low data points could come from a large-scale underdensity in the COSMOS field at this redshift. The Le Borgne et al. (2009) model overpredicts the contribution of the 24 μm sources at z>1. The Valiante et al. (2009) model does not reproduce the trend of these measurements. Franceschini et al. (2010) underestimate the contribution of the local sources and overestimate the contribution of z∼1 sources.

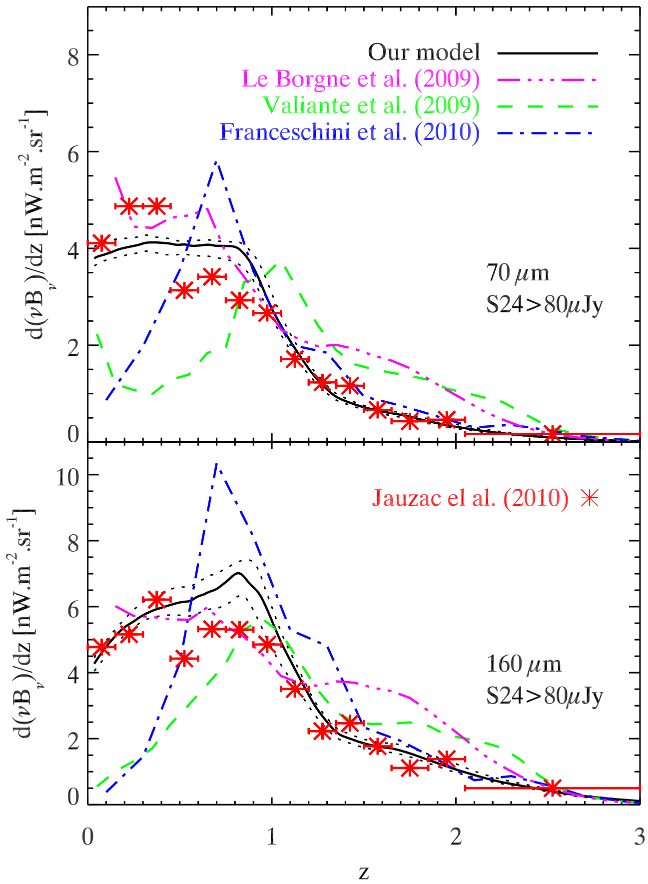

Figure 8. Differential contribution of the $S_{24} > 80$ μJy sources to the CIB as a function of the redshift at 70 μm (upper panel) and 160 μm (lower panel). *Red asterisks*: measurement by stacking in the COSMOS field (Jauzac et al. 2010). *Black solid line*: Our model (1-σ limit in *black dotted line*). *Purple three dot-dashed line*: Le Borgne et al. (2009) model. *Green dashed line*: Valiante et al. (2009) model. *Blue dot-dashed line*: Franceschini et al. (2010) model.

5.6. Comparison with the measured Poisson fluctuations of the CIB

Table 3 summarizes the recent measurements of the non-correlated fluctuations of the CIB (P_{SN}) and the predictions of our model. Note that P_{SN} depends strongly on the $S_{\nu,cut}$, the flux density at which the resolved sources are cleaned. We agree with the measurements of Miville-Deschênes et al. (2002) at 60 μm and 100 μm, Lagache et al. (2007) at 160 μm and Viero et al. (2009) at 250 μm and 350 μm. We found a value 35% lower than Viero et al. (2009) at 500 μm. This is consistent with the slight under-estimation of the counts at 500 μm by our model. Our model is also about 40% lower than the SPT

wavelength μm	reference	S_{cut} mJy	$P_{SN,mes}$ $Jy^2.sr^{-1}$	$P_{SN,model}$ $Jy^2.sr^{-1}$	$<z_{model}>$
60	Miville-Deschênes et al. (2002)	1000	1600±300	2089±386	0.20±0.01
90	Matsuura et al. (2010)	20	360±20	848±71	0.79±0.03
100	Miville-Deschênes et al. (2002)	700	5800±1000	7364±1232	0.38±0.03
160	Lagache et al. (2007)	200	9848±120	10834±3124	0.73±0.06
250	Viero et al. (2009)	500	11700±400	11585±2079	0.81±0.08
350	Viero et al. (2009)	400	6960±200	5048±1083	1.17±0.12
500	Viero et al. (2009)	-	2630±100	1677±484	1.59±0.21
1363	Hall et al. (2010)	15	17±2	10±3	4.07±0.24

Table 3. Level of the non-correlated fluctuations of the CIB at different wavelengths and comparison with the predictions of the model. The uncertainties on the model predictions take into account the uncertainties on γ_b. The mean redshift $<z_{model}>$ of the contribution to the fluctuations is a prediction of the model.

measurements at 1.36 mm (Hall et al. 2010). It could be due to a lack of faint sources at high redshift in our model. We also disagree with Matsuura et al. (2010) at 90 μm within a factor of 2. Nevertheless, they cleaned all the detected sources without fixed cut in flux. We took their "mean" value of 20 mJy for the flux cut. The high sensitivity of the measurements of the flux cut could thus explains this difference (for instance, a decrease of the flux cut by 25% implies a decrease of the fluctuations of 19%).

We also computed the mean redshift at which the fluctuations are emitted with

$$< z >= \frac{\int_0^\infty z \frac{dP_{SN}}{dz} dz}{\int_0^\infty \frac{dP_{SN}}{dz} dz}. \quad (21)$$

The results are written in Table 3. As expected, the mean redshift increases with the wavelength. Studying the long wavelengths is thus very useful to probe high redshift populations.

5.7. Comparison with the pixel histogram of the BLAST maps

The quality of our counts at low fluxes in the sub-mm range can be tested using a P(D) analysis (Condon 1974; Patanchon et al. 2009; Glenn et al. 2010). Without instrumental noise, the probability density of the signal in a pixel of the map, P(D), is given by:

$$P(D) = \int_0^\infty \left[exp\left(\int_0^\infty R(x) e^{i\omega x} dx - \int_0^\infty R(x) dx \right) \right] e^{-i\omega D} d\omega \quad (22)$$

where R(x) is defined by

$$R(x) = \int \frac{1}{b} \frac{dN}{dS_\nu} \left(\frac{x}{b} \right) d\Omega. \quad (23)$$

This probability distribution must be convolved by the distribution of the instrumental noise. We also subtract the mean of this distribution.

We tested our model with the deepest part of the observations of the CDFS by the BLAST team. We kept only the pixels of the map with a coverage larger than 90% of the maximum coverage. We smoothed the signal, noise and beam map by a gaussian kernel with the same full width at half maximum than the BLAST beam. This smoothing reduces the effect of the instrumental noise Patanchon et al. (2009). The predictions of our model and the BLAST pixel histograms at 250 μm, 350 μm and 500 μm are shown in Fig. 9. The uncertainties on the model predictions take into account the BLAST calibration uncertainties (Truch et al. 2009). The model agrees rather well with the data. Nevertheless the measured histogram is slightly larger than the predictions of the model, especially at 500 μm. It is consistent with the slight under-estimation by our model of the counts at 500 μm (the higher the counts, the larger the histogram). The clustering of the galaxies (negliged in this analysis) tends to enlarge the histogram of about 10% and could also contributes to this disagreement (Takeuchi & Ishii 2004; Patanchon et al. 2009; Glenn et al. 2010). The Valiante et al. (2009) model fits very well fit the BLAST pixel histograms. Le Borgne et al. (2009) and Franceschini et al. (2010) overpredicts the number of bright pixels at 250 μm and 350 μm (S_ν >50mJy). It is consistent with the fact that they overpredict the counts at high flux (Oliver et al. 2010; Glenn et al. 2010).

5.8. Degeneracies between parameters

The Pearson correlation matrix of our model is given in Tab. 4. We found a very strong anticorrelation between σ and $L_\star$(z=0) (-0.90) and between $L_\star$(z=0) and $\phi_\star$(z=0) (-0.85). These classical strong correlations are due to the choice of the parametrisation of the LF. There are also very strong degeneracies between the evolution in density and in luminosity of the LF (-0.81 between 0 and the first break, -0.67 between the two breaks and -0.76 after the second break).

There are also some slight degeneracies between the calibration factors. The *Spitzer* calibration parameters are correlated (0.68 between 24 μm and 70 μm, 0.73 between 24 μm and 160 μm, 0.62 between 70 μm and 160 μm). The other correlation implying a calibration factor are between -0.6 and 0.6.

The marginalized probability distributions of each parameter and the 1, 2, and 3-σ confidence regions for each pair of parameters are plotted Fig. 10. Some distributions are not Gaussian. It thus justifies the use to use a MCMC algorithm.

6. Interpretation of the results

6.1. Evolution of the luminosity function

Our model uses a very strong evolution of the bolometric infrared luminosity function to reproduce the infrared observations. The characteristic luminosity ($L_\star$) strongly decreases since z=2 to now. This parameter has been divided by about a factor 50 from z=2 to 0. The characteristic density ($\phi_\star$) increases strongly between z=2 and z=1 and slightly decreases between z=1 and now. At z>2, the model is compatible with no evolution in luminosity and a slight decrease of the density when

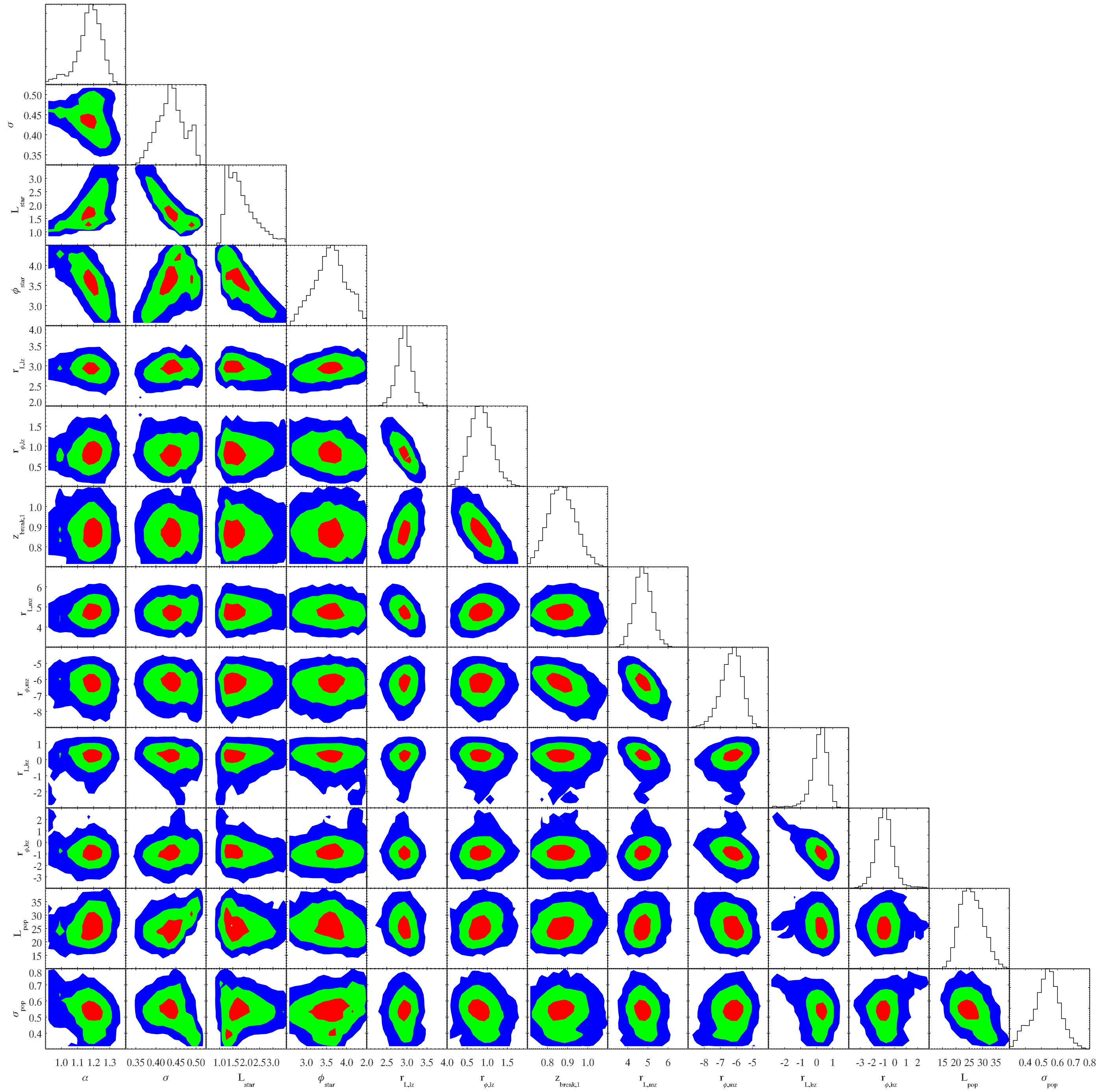

Figure 10. *Diagonal plots*: marginalized probability distributions of each parameters deduced from the MCMC. *Non-diagonal plots*: 1-σ (*red*), 2-σ (*green*) and 3-σ (*blue*) regions for each pair of parameters). *From left to right:* α, σ, $L_\star$, $\phi_\star$, $r_{L_\star,lz}$, $r_{phi_\star,lz}$, $z_{break,1}$, $r_{L_\star,mz}$, $r_{phi_\star,mz}$, $r_{L_\star,hz}$, $r_{phi_\star,hz}$, L_{pop} and σ_{pop} (c.f. Table 1).

the redshift increases. The evolution of these two parameters are plotted in Fig. 11.

We compared our results with Caputi et al. (2007) measurements performed from MIPS 24 μm observations and Magnelli et al. (2009) measurement obtained using MIPS 70 μm observations. These two works used a stacking analysis to measure the faintest points. The evolutions of $L_\star$ and $\phi_\star$ only marginally agrees with these two works. Nevertheless, they use different fixed values of σ and α and an extrapolation from the monochromatic luminosity to L_{IR}. These choices could imply some biases. We found as Caputi et al. (2007) a strong negative evolution in density between z$\sim$1 and z$\sim$2. They found an evolution in $(1+z)^{-3.9\pm1.0}$ and we found $(1+z)^{-6.2\pm0.5}$. Nevertheless, our value is probably biased by our non-smooth parametrization. This evolution is discussed in details by

	α	σ	$L_\star$(z=0)	$\phi_\star$ (z=0)	$r_{L_\star,lz}$	$r_{phi_\star,lz}$	$z_{break,1}$	$r_{L_\star,mz}$	$r_{phi_\star,mz}$	$r_{L_\star,hz}$	$r_{phi_\star,hz}$	L_{pop}	σ_{pop}
α	1.00	-0.48	0.71	-0.75	0.02	-0.06	0.04	0.14	-0.16	-0.04	0.11	-0.02	0.05
σ	-0.48	1.00	-0.90	0.62	-0.03	0.15	-0.06	0.10	0.05	-0.20	0.12	0.48	-0.37
$L_\star$(z=0)	0.71	-0.90	1.00	-0.85	-0.14	-0.03	0.07	0.00	-0.11	0.11	-0.04	-0.19	0.20
$\phi_\star$ (z=0)	-0.75	0.62	-0.85	1.00	0.22	-0.15	-0.05	0.04	0.08	-0.04	-0.09	-0.11	-0.01
$r_{L_\star,lz}$	0.02	-0.03	-0.14	0.22	1.00	-0.81	0.51	-0.44	0.10	0.14	-0.12	-0.27	0.13
$r_{phi_\star,lz}$	-0.06	0.15	-0.03	-0.15	-0.81	1.00	-0.78	0.18	0.07	-0.08	0.13	0.18	-0.17
$z_{break,1}$	0.04	-0.06	0.07	-0.05	0.51	-0.78	1.00	0.05	-0.51	-0.09	0.07	0.12	0.12
$r_{L_\star,mz}$	0.14	0.10	0.00	0.04	-0.44	0.18	0.05	1.00	-0.67	-0.43	0.29	0.05	-0.09
$r_{phi_\star,mz}$	-0.16	0.05	-0.11	0.08	0.10	0.07	-0.51	-0.67	1.00	0.35	-0.41	-0.04	-0.07
$r_{L_\star,hz}$	-0.04	-0.20	0.11	-0.04	0.14	-0.08	-0.09	-0.43	0.35	1.00	-0.76	-0.20	-0.26
$r_{phi_\star,hz}$	0.11	0.12	-0.04	-0.09	-0.12	0.13	0.07	0.29	-0.41	-0.76	1.00	0.11	0.18
L_{pop}	-0.02	0.48	-0.19	-0.11	-0.27	0.18	0.12	0.05	-0.04	-0.20	0.11	1.00	-0.39
σ_{pop}	0.05	-0.37	0.20	-0.01	0.13	-0.17	0.12	-0.09	-0.07	-0.26	0.18	-0.39	1.00

Table 4. Pearson correlation matrix for our model. The part of the matrix concerning the calibration factors is not written to save space.

Caputi et al. (2007).

Reddy et al. (2008) claimed that $\alpha \sim 1.6$ at z>2. But, we do not need an evolution of α and σ to reproduce the observations. Nevertheless, the infrared measurements are not sufficiently deep to constraint accurately an evolution of α.

6.2. Evolution of the dust-obscured star formation rate

The bolometric infrared luminosity density (ρ_{IR}) can be deduced from the bolometric infrared LF. Our local value of ρ_{IR} ((1.05±0.05)×10^8 L$_\odot$.Mpc^{-3}) agrees with Vaccari et al. (2010) measurements ($1.31^{+0.24}_{-0.21}\times10^8$ L$_\odot$.Mpc^{-3}). We also agree well with measurements at higher redshift (Rodighiero et al. (2009) and Pascale et al. (2009) (see Fig. 12). ρ_{IR} can be converted into star formation rate density (SFRD) using the conversion factor $1.7\times10^{-10}\,M_\odot.yr^{-1}.L_\odot^{-1}$ (Kennicutt 1998). The SFRD derived from our model agrees rather well with the Hopkins & Beacom (2006) fit of the optical and infrared measurements.

We also determined the contribution of the different ranges of luminosity (normal: $L_{IR} < 10^{11}\,L_\odot$, LIRG: $10^{11} < L_{IR} < 10^{12}\,L_\odot$, ULIRG:$10^{12} < L_{IR} < 10^{13}\,L_\odot$, HyLIRG: $L_{IR} > 10^{13}\,L_\odot$). Between z=0 and 0.5, the infrared luminosity density is dominated by normal galaxies ($L_{IR} < 10^{11}\,L_\odot$). Their contribution decreases slowly with redshift due to the evolution of the LF seen in Fig. 11. Between z=0.5 and 1.5, the infrared output is dominated by the LIRG. At higher redshift, it is dominated by ULIRGs. The HyLIRGs never dominate and account for some percent at high redshift. A physical cutoff at very high luminosity thus would not change strongly the infrared density evolution.

Following our model, the number of very bright objects (> $10^{12.5}$ $L_\odot$) is maximal around z=2 (see Fig. 11). These objects could be very massive galaxies observed during their formation in the most massive dark matter halos. Among other analysis, the study of the spatial distribution of the galaxies will help to confirm or infirm this scenario (Penin et al. 2010).

Around z=1, the number of very bright objects is lower than at higher redshift, but the number of LIRGs is about one order of magnitude larger. From z=1 to now, the infrared output has decreased by about one order of magnitude. Our model makes only a description of this evolution and we need physical models to understand why, contrary to nowadays, the star formation at high redshift is dominated by few very-quickly-star-forming galaxies, when the associated dark matter halos grew by hierarchical merging (Cole et al. 2000; Lanzoni et al. 2005). We also need an explanation of the decrease of the star formation since z=1. The main candidates the feedback of AGNs and starbursts (e.g. Baugh (2006)) and/or the lack of gas.

6.3. CIB SED

The value of the CIB at different wavelengths predicted by the model is given in Table 5. We found a CIB integrated value (over the 8-1000 μm range) of 23.7±0.9 nW.m^{-2}.sr^{-1}. It agrees with the 24-27.5 nW.m^{-2}.sr^{-1} range of Dole et al. (2006).

We compared the CIB spectrum found with our model with the measurements (see Fig. 13). Our model is always higher than the lower limit given by the stacking. The Marsden et al. (2009) limits are very stringent. Nevertheless, they could be overestimated due to the contamination due to clustering (Bavouzet 2008; Fernandez-Conde et al. 2010; Béthermin et al. 2010b). Our model is compatible with the upper limit given by the absorption of the TeV photons by photon-photon interaction with the CIB (see Sect. 7.2). We globally agree with the DIRBE/WHAM (Lagache et al. 2000) and Akari (Matsuura et al. 2010) absolute measurement, excepting at 90 μm (Akari) and 100 μm (DIRBE/WHAM) where the measurements are significantly higher than our model. These measurements need an accurate subtraction of the zodiacal light and of the galactic emissions and an accurate inter-calibration between DIRBE and FIRAS. Indeed, a bad removal of the zodiacal light explains this disagreement (Dole et al. 2006). At larger wavelengths, we very well agree with the FIRAS absolute measurements of Lagache et al. (2000).

We separated the contribution of the infrared galaxies to the CIB in 4 redshift slices, each slice corresponding to about a quarter of the age of the Universe (Fig. 13). Between 8 and 30 μm, we can see a shaky behavior of each slice due to the PAH emission bands. The total is smoother. The $0 < z < 0.3$ dominates the spectrum only near 8 μm due to the strong PAH emission at this rest-frame wavelength. This slice, where the infrared luminosity density is the lowest, has a minor contribution at the other wavelengths. The $0.3 < z < 1$ slice dominates the spectrum between 10 and 350 μm. The sub-mm and mm wavelengths are dominated by the sources lying at higher redshift ($z > 2$, see Lagache et al. (2005)). It is due to redshift effects that shift the

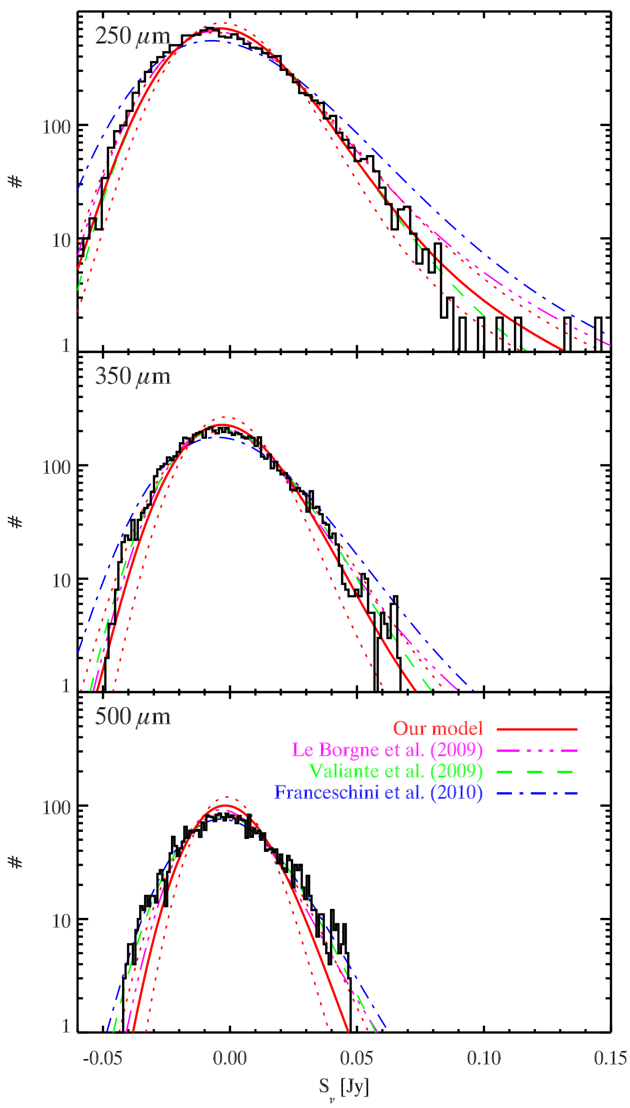

Figure 9. Comparison with the BLAST pixel histogram at 250 μm (*upper panel*), 350 μm (*middle panel*) and 500 μm (*lower panel*). (*Black histogram*): histogram of the values of the central part of the BLAST beam-smoothed map in Jy/beam. (*Red solid line*): distribution predicted by our model using a P(D) analysis. Our analysis does not include the clustering. *Purple three dot-dashed line*: Le Borgne et al. (2009) model. *Green dashed line*: Valiante et al. (2009) model. *Blue dot-dashed line*: Franceschini et al. (2010) model.

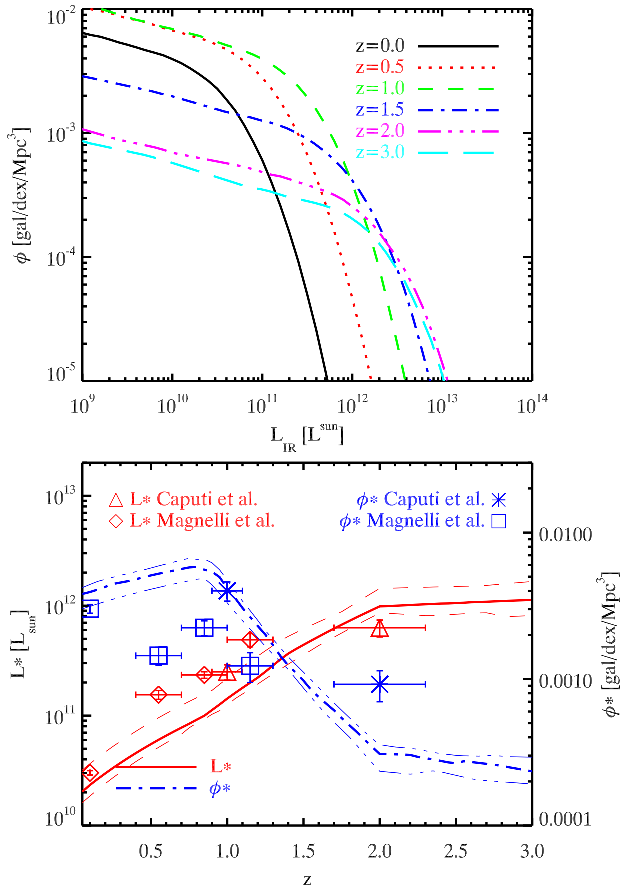

Figure 11. Evolution of the bolometric infrared luminosity function with the redshift. Upper panel: bolometric LF at z=0 (*solid line*), z=0.5 (*dot line*), z=1(*dashed line*), z=1.5 (*dot-dash line*), z=2 (*3-dot-dash line*), z=3 (*long dashed line*). Lower panel: Evolution of the $L_\star$ (*red solid line*) and $\phi_\star$ (*blue dot-dash line*) parameter as a function of redshift and 1-σ confidence region. The measurement of $L_\star$ by Caputi et al. (2007) (*triangles*) using 24 μm obervations and Magnelli et al. (2009) (*diamonds*) using 70 μm observations are plotted in *red*. The measurement of $\phi_\star$ by Caputi et al. (2007) (*cross*) and Magnelli et al. (2009) (*square*) are in *blue*.

peak of emission around 80 μm rest-frame to the sub-mm. The mean redshift of the contribution to the CIB is written in Table 5 and computed with

$$<z>=\frac{\int_0^\infty z\frac{dB_\nu}{dz}dz}{\int_0^\infty \frac{dB_\nu}{dz}dz} \tag{24}$$

We also separate the contribution of the different infrared luminosity classes. The normal galaxies and LIRGs dominate the background up to 250 μm. It is compatible with the fact that these populations are dominant at low redshift. At larger wavelengths, the redshift effects tend to select high redshift sources; LIRGs and ULIRGs are responsible for about half of the CIB each. The HyLIRG have only a small contribution (< 10%) including in the mm range (Fig. 13, bottom).

7. Predictions

7.1. Confusion limit

The confusion limit can be defined in several ways. The radioastronomers use classically a source density criteria, where the confusion limit is the flux cut for which a critical density of source is reached. The choice of this critical density is not trivial. We follow the approach of Dole et al. (2003). The source density limit N_{SDC} is reached when there is a probability P to have an other source in a k θ_{FWHM} radius (where θ_{FWHM} is the full width at half maximum of the beam profile). Dole et al. (2003) show that

$$N_{SDC}=-\frac{log(1-P)}{\pi k^2\theta_{FWHM}^2} \tag{25}$$

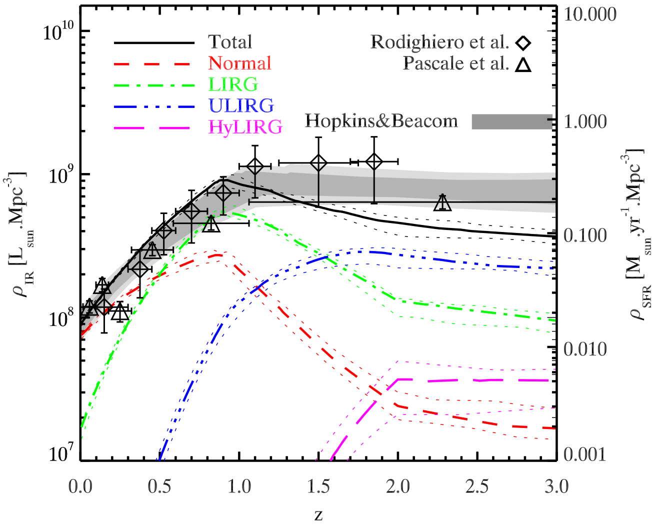

Figure 12. Evolution of the bolometric infrared luminosity density (*black solid line*) as a function of the redshift. The contribution of normal galaxies ($L_{IR} < 10^{11} L_\odot$), LIRG($10^{11} < L_{IR} < 10^{12} L_\odot$), ULIRG($10^{12} < L_{IR} < 10^{13} L_\odot$), HyLIRG($L_{IR} > 10^{13} L_\odot$) are plotted with *short-dahsed*, *dot-dash*, *three-dot-dash*, *long-dashed line* respectively. The measurements of Rodighiero et al. (2009) using the MIPS 24 μm data are plotted with *diamonds* and Pascale et al. (2009) ones using a BLAST stacking analysis with *triangles*. The Hopkins & Beacom (2006) fit of the optical and infrared measurement is plotted with a *dark grey area* (1-σ) and a *light grey area* (3-σ).

wavelength μm	CIB nW.m^{-2}.sr^{-1}	CIB MJy.sr^{-1}	<z>
15	$3.294^{+0.105}_{-0.128}$	$0.016^{+0.001}_{-0.001}$	$0.820^{+0.026}_{-0.018}$
24	$2.596^{+0.076}_{-0.139}$	$0.021^{+0.001}_{-0.001}$	$0.894^{+0.025}_{-0.029}$
70	$5.777^{+0.165}_{-0.067}$	$0.135^{+0.004}_{-0.002}$	$0.773^{+0.022}_{-0.021}$
100	$9.014^{+0.231}_{-0.125}$	$0.300^{+0.008}_{-0.004}$	$0.829^{+0.023}_{-0.024}$
160	$11.771^{+0.382}_{-0.318}$	$0.628^{+0.020}_{-0.017}$	$0.947^{+0.032}_{-0.019}$
250	$9.100^{+0.395}_{-0.382}$	$0.758^{+0.033}_{-0.032}$	$1.124^{+0.053}_{-0.021}$
350	$5.406^{+0.190}_{-0.417}$	$0.631^{+0.022}_{-0.049}$	$1.335^{+0.075}_{-0.060}$
500	$2.237^{+0.077}_{-0.217}$	$0.373^{+0.013}_{-0.036}$	$1.680^{+0.124}_{-0.122}$
850	$0.374^{+0.057}_{-0.042}$	$0.106^{+0.016}_{-0.012}$	$2.444^{+0.292}_{-0.192}$
1100	$0.139^{+0.031}_{-0.017}$	$0.051^{+0.011}_{-0.006}$	$2.833^{+0.341}_{-0.201}$

Table 5. Surface brightness of the CIB and mean redshift <z> of the contribution to the CIB at different wavelengths as predicted by the model.

We chose P = 0.1 and k = 0.8 following Dole et al. (2003).

This source density criterion does not take into account the contributions of the sources fainter than the flux limit. We made also an estimate of the photometric confusion noise based on the P(D) analysis (see Sect. 5.7). The P(D) distribution in absence of instrumental noise is not gaussian and have a large tail at bright flux. Thus the standard deviation is not a good estimator of the confusion noise. We chose to compute the interquartile interval of the P(D) divided by 1.349. With this definition, the value of the confusion noise is exactly σ in the Gaussian case, and we are less sensitive to the bright outliers.

These two estimators can be computed from the counts predicted by our model. We assume that the sources are point-like. The confusion noise found for large telescope at short wavelength (<8 μm for a 0.85 m-diameter telescope like *Spitzer* and <35 μm for a 3.29 m-diameter telescope like *Herschel*) are thus underestimated. For this reason, we do not estimate the confusion levels for beam smaller than 2 arcsec.

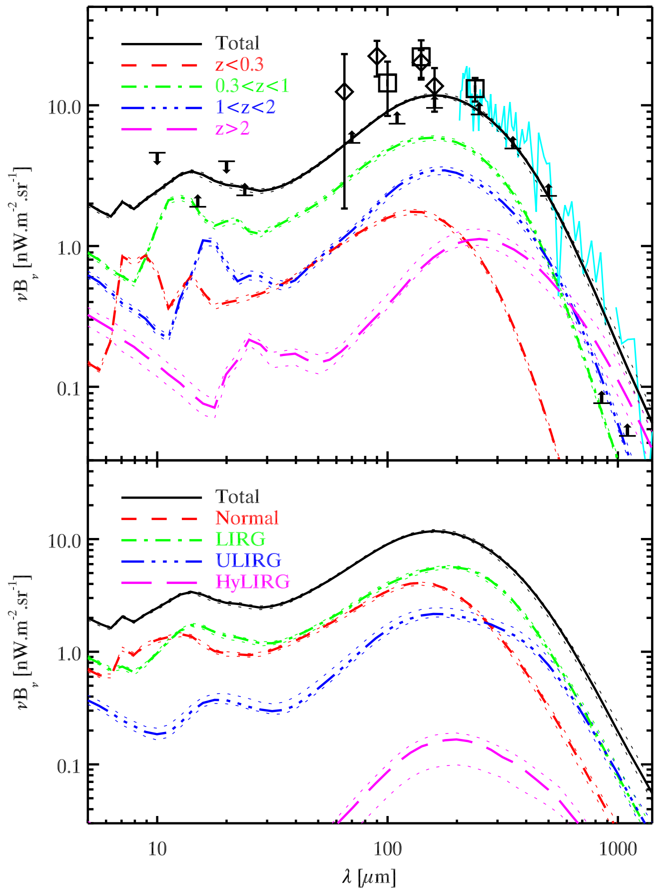

Figure 13. Upper panel: contribution to the CIB per redshift slice. *Black solid line*: CIB spectrum predicted by the model. *Red short-dashed line*: Contribution of the galaxies between z=0 and 0.3. *Green dot-dash line*: Same thing between z=0.3 and 1. *Blue three dot-dash line*: same thing between z=1 and 2. *Purple long-dashed line*: Contribution of the galaxies at redshift larger than 2. *Black arrows*: Lower limits coming from the number counts at 15 μm (Hopwood et al. 2010) and 24 μm (Béthermin et al. 2010a) and the stacking analysis at 70 μm (Béthermin et al. 2010a), 100 μm, 160 μm (Berta et al. 2010), 250 μm, 350 μm, 500 μm (Marsden et al. 2009), 850 μm (Greve et al. 2009) and 1.1 mm (Scott et al. 2010) and upper limits coming from absorption of the TeV photons of Stecker & de Jager (1997) at 20 μm and Renault et al. (2001) between 5 μm and 15 μm. *Black diamonds*: Matsuura et al. (2010) absolute measurements with Akari. *Black square*: Lagache et al. (2000) absolute measurements with DIRBE/WHAM. *Cyan line*: Lagache et al. (2000) FIRAS measurement.
Lower panel: Contribution of to the CIB of the normal galaxies (*red short-dashed line*), LIRGs (green dot-dash line), ULIRGs (*blue three dot-dash line*) and HyLIRG (*purple long-dashed line*) and all the galaxies (*black solid line*).

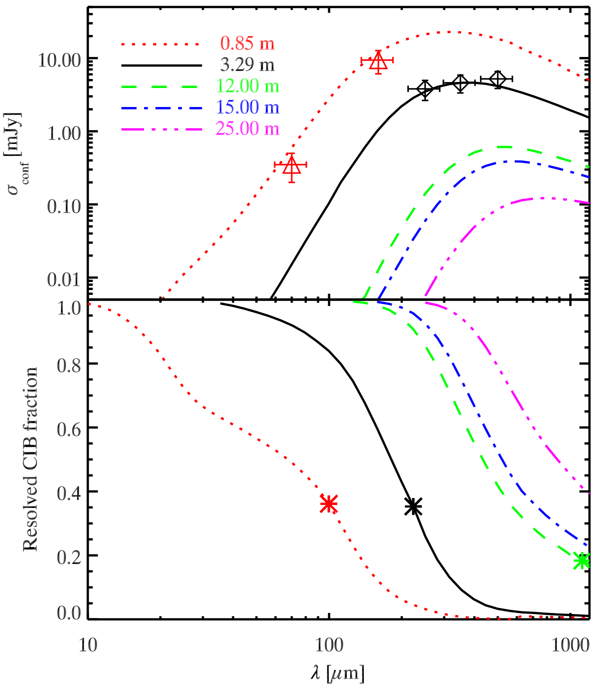

Figure 14. Upper panel: 1-σ confusion noise as a function of the wavelength for different telescope diameters. We use the confusion noise given by the P(D) method (see Sect. 7.1) for this plot. *Red triangles*: Frayer et al. (2009) *Spitzer*/MIPS confusion measurements. *Black diamonds*: Nguyen et al. (2010): *Herschel*/SPIRE confusion noise measurements (5-σ_{conf} cut). Lower panel: Resolved fraction of the CIB by sources brighter than 5-σ confusion noise (fluctuations) and the source density limit.
Both panel: *Red dotted line*: Telescope with a diameter of 0.85 m like Spitzer. *Black solid line*: 3.29 m telescope like *Herschel*. *Green dashed line*: 12 m telescope like Atacama pathfinder experiment (APEX). *Blue dot-dashed line*: 15 m telescope like the CSO. *Purple three dot-dashed line*: 25 m like the CCAT project. *Asterisks*: Transition between the source density limitation (short wavelengths) and the fluctuation limitation (long wavelengths).

The Fig. 14 (upper panel) represents the confusion noise. It agrees with the confusion noise measured by Frayer et al. (2009) and Nguyen et al. (2010) with *Spitzer*/MIPS and *Herschel*/SPIRE. Weiß et al. (2009) estimate that the confusion noise for a APEX/LABOCA map smoothed by the beam is 0.9 mJy/beam. We find 0.6 mJy/beam with the P(D) approach.

We also compute the resolved fraction of the CIB by sources brighter than the confusion limit of Dole et al. (2003) (source density criterion) and the 5-σ_{conf} given by the P(D). Fig. 14 (lower panel) and Table 6, 7, 8, 9 and 10 summarize the results. The transition in the confusion regime between the source density limitation (short wavelengths) and the fluctuation limitation (long wavelengths) happens at 100 μm for *Spitzer*, 220 μm for *Herschel* and 1120 μm for the CSO (asterisks in the lower panel of Fig. 14). For larger antennas below 1.2 mm, the confusion is mainly due to the source density.

According to these results, at the confusion limit, *Herschel* can resolve 92%, 84%, 60%, 25.9%, 9.2% and 3.3% of the CIB at 70 μm, 100 μm, 160 μm, 250 μm, 350 μm and 500 μm respectively. Nevertheless, due to the blackbody emission of the telescope (about 60 K), very long integration times are needed to reach the confusion limit at short wavelengths. The confusion limit in PACS will be reach only in the ultra-deep region of the H-GOODS survey. The confusion limit will probably be never reached at 70 μm. A telescope with the same size as *Herschel* and a cold (5K) mirror, like SPICA, could resolve almost all the CIB from the mid-infrared to 100 μm. A 25 m single-dish sub-mm telescope like the Cornell Caltech Atacama telescope (CCAT) project would be able to resolve more than 80% of the CIB up to 500 μm.

7.2. High energy opacity

The CIB photons can interact with TeV photons. The cross section between a E_γ rest-frame high-energy photon and an infrared photon with a observer-frame wavelength λ_{IR} interacting at a redshift z with an angle θ (and $\mu = cos(\theta)$) is (Heitler 1954; Jauch & Rohrlich 1976)

$$\sigma_{\gamma\gamma}(E_\gamma, \lambda_{IR}, \mu, z) = H\left(1 - \frac{\epsilon_{th}}{\epsilon}\right)\frac{3\sigma_T}{16}(1-\beta^2)\times \tag{26}$$

$$\left[2\beta(\beta^2-2) + (3-\beta^4)ln\left(\frac{1+\beta}{1-\beta}\right)\right] \tag{27}$$

with

$$\beta = \sqrt{1 - \frac{\epsilon_{th}}{\epsilon}}, \tag{28}$$

$$\epsilon_{th}(E_\gamma, \mu, z) = \frac{2(m_e c^2)^2}{E_\gamma(1-\mu)(1+z)}, \tag{29}$$

$$\epsilon(\lambda_{IR}, z) = \frac{hc(1+z)}{\lambda_{IR}}, \tag{30}$$

where σ_T is the Thompson cross section (6.65×10^{-29} m^2), m_e the mass of the electron and H the Heaviside step function (H(x)=1 if x>0 and 0 else).

The optical depth $\tau(E_\gamma, z_s)$ for a photon observed at energy E_γ and emitted at a redshift z_s can be easily computed (Dwek & Krennrich 2005; Younger & Hopkins 2010; Dominguez et al. 2010) with

$$\tau(E_\gamma, z_s) = \int_0^{z_s} dz \frac{D_H}{\sqrt{\Omega_\Lambda + (1+z)^3\Omega_m}} \tag{31}$$

$$\int_{-1}^{1} d\mu \frac{1-\mu}{2} \int_{5\mu m}^{\infty} d\lambda_{IR} n_{\lambda_{IR}}(\lambda_{IR}, z)(1+z)^2 \sigma_{\gamma\gamma}(E_\gamma, \lambda_{IR}, \mu, z) \tag{32}$$

where $n_{\lambda_{IR}}(\lambda_{IR}, z)$ is the comoving number density of photons emitted at a redshift greater than z between λ_{IR} and $\lambda_{IR} + d\lambda_{IR}$. The 5 μm cut corresponds to the limit of the validity of our model. The number density of photons is computed with

$$n_{\lambda_{IR}}(\lambda_{IR}, z) = \frac{4\pi}{hc\lambda_{IR}}(B_{\nu,CIB} + B_{\nu,CMB}) \tag{33}$$

where $B_{\nu,CIB}$ is the CIB given by our model and $B_{\nu,CMB}$ is the brightness of a blackbody at 2.725K corresponding to the cosmic microwave background (Fixsen 2009). Our predicted opacities do not take into account the absorption by the cosmic optical background photons (COB, $\lambda < 5$ μm). Younger & Hopkins (2010) showed that the contribution of the COB to the opacity is negligible for energies larger than 5 TeV.

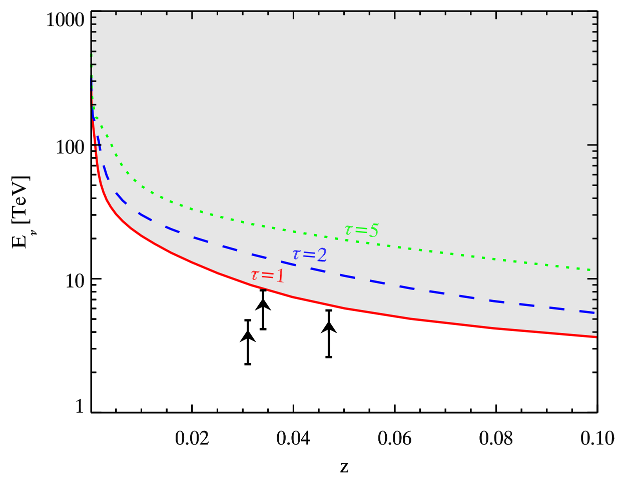

Figure 15. Fazio-Stecker relation: energy at which the opacity reach a given τ as a function of redshift. This plot is done for $\tau = 1$ (*red solid line*), 2 (*blue dashed line*) and 5 (*green dotted line*). The data points are the cutoff energy of Mkn 501 (Aharonian et al. 1999), Mkn 421 (Aharonian et al. 2002) and Lac 1ES 1959+650 (Aharonian et al. 2003).

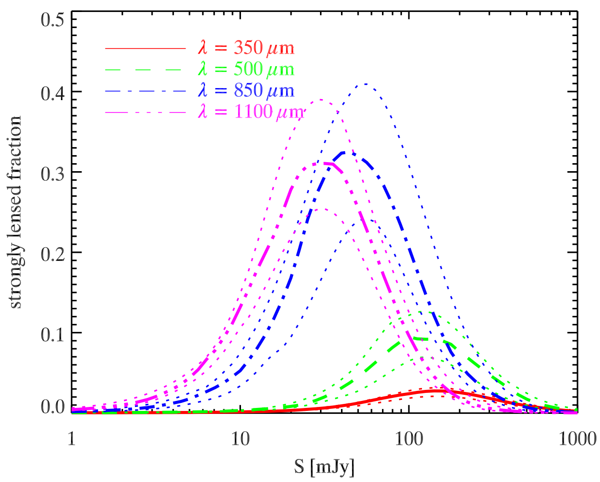

Figure 16. Fraction of strongly lensed sources (magnification larger than 2) as a function of the flux at 350 μm (*red solid line*), at 500 μm (*green dashed line*), at 850 μm (*blue dot-dashed line*) and at 1.1 mm (*purple three-dot-dashed line*). The *dotted lines* represent the 1-σ confidence area of our model.

We can determine up to which redshift the opacity stays lower than 1. We can thus define an horizon as a function of the energy, called Fazio-Stecker relation. We can see in Fig. 15 that the observed energy cutoff of low-redshift blazars (Mkn 501 (Aharonian et al. 1999), Mkn 421 (Aharonian et al. 2002) and BL Lac 1ES 1959+650 (Aharonian et al. 2003)) is compatible with this relation.

7.3. Effect of the strong lensing on the number counts

The strongly-lensed fraction is the ratio between the counts of lensed sources and the total observed counts. Because the slope of the counts varies a lot with the flux and wavelength, this fraction depends on the flux and the wavelength (see Fig. 16). The strongly lensed fraction is always smaller than 2% below 250 μm and is thus negligible. At larger wavelengths, we predict a maximum of the strongly lensed fraction near 100 mJy. At 500 μm, about 15 % of the sources brighter than 100 mJy are lensed. This fraction increases to 40% near 1 mm.

Our results can be compared with ones of Negrello et al. (2007) model. The two model predict that the lensed fraction as a function of the flux is a bump around 100 mJy. But, the amplitude of this bump predicted by the two models is significantly different. For instance, the maximum of the lensed fraction at 500 μm is 15% for our model and 50% for the Negrello et al. (2007) model. The slope between 10 and 100 mJy is steeper in Negrello et al. (2007) model than in ours and is incompatible with the measurements (Clements et al. 2010; Oliver et al. 2010; Glenn et al. 2010). The steeper the slope, the larger the lensed fraction. This explains why the Negrello et al. (2007) model predicts larger lensed fraction than ours. The probability for a source to be lensed increases with its redshift. Differences in the redshift distributions of the models could also explain some differences in the lensed fraction.

The Fig. 6 shows the respective contribution of the lensed and non-lensed sources to the SPT counts of dusty sources without IRAS 60 μm counterparts at 1.38 mm (Vieira et al. 2009). According to the model, these counts are dominated by strongly-lensed sources above 15 mJy. These bright sources are thus very good candidates of strongly-lensed sub-mm galaxy.

We made predictions on the contribution of the strongly-lensed sources to the *Planck* number counts (see Fig. 17). We use the Fernandez-Conde et al. (2008) 5-σ limits, because they take into account the effect of the clustering on the confusion noise. This effect is non-negligible due to the large beam of *Planck*. We found that the contribution of the lensed sources to the *Planck* counts is negligible in all the bands (a maximum of 0.47 galaxies.sr^{-1} at 550 μm). At high redshift, *Planck* will probably detect more small structures like proto-clusters, than individual galaxies. *Planck* is thus not the best survey to find lensing candidates. Sub-mm surveys with a sensitivity near 100 mJy are more efficient. For instance, the *Herschel*-ATLAS survey should found 153±26 and 411±24 lensed sources with S_{500} >50 mJy and S_{350} >50 mJy, respectively, on 600 deg^2.

8. Discussion

8.1. Comparison with other backwards evolution models

The evolution of the infrared luminosity density predicted by our model can be compared with the prediction of the recent backwards evolution models. We find, like Franceschini et al. (2010), a strong increase of ρ_{IR} from z=0 to z=1, a break around z=1, and a decrease at larger redshift. On the contrary, the Valiante et al. (2009) and Le Borgne et al. (2009) models predict a maximum of infrared luminosity density around z=2.

As Le Borgne et al. (2009) and Franceschini et al. (2010), we found that LIRGs dominate infrared luminosity density

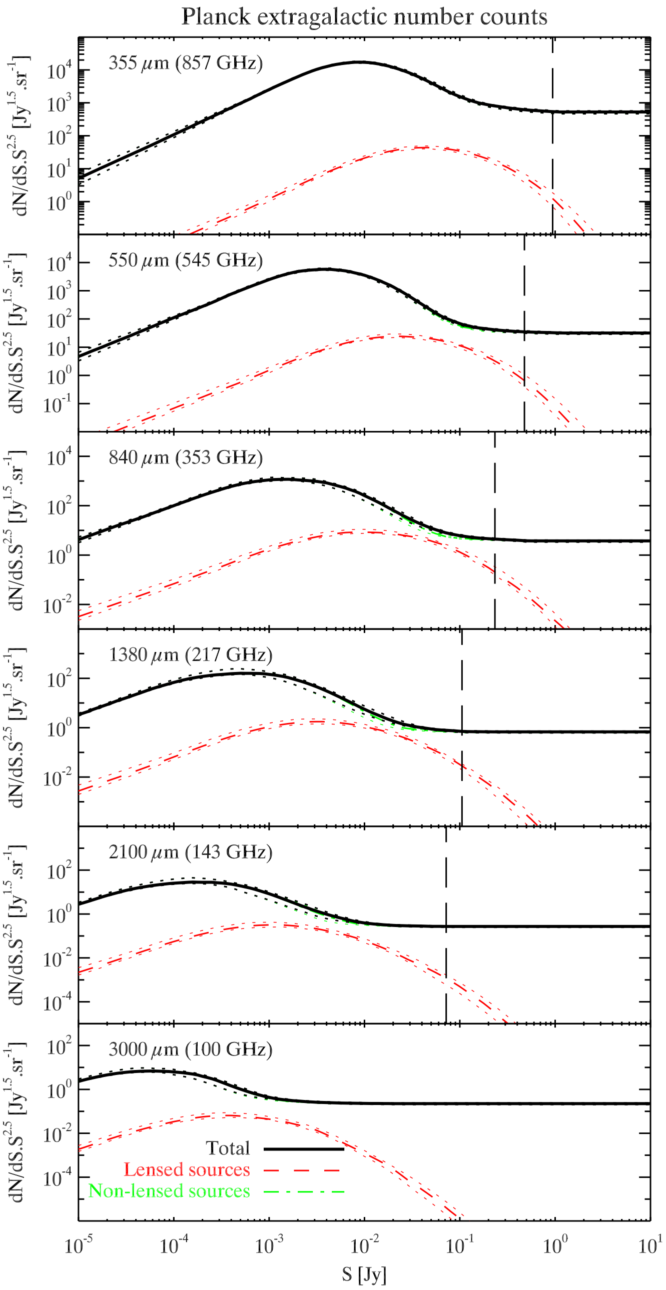

Figure 17. Differential number counts in the *Planck* bands. These counts takes only into account the individual star forming galaxies. *Black solid line*: Total contribution. *Green dot-dashed line*: Contribution of the non-lensed sources. *Red dashed line*: Contribution of the strongly-lensed sources. *Dotted lines* 1-σ contours. *Vertical long-dahsed line*: 5-σ limits (confusion+instrumental) of Fernandez-Conde et al. (2008) for a bias of 1.5.

around z=1 and that ULIRG dominate at redshift larger than 1.5. We also found as Le Borgne et al. (2009) that normal galaxies dominates only up to z~0.5.

The Valiante et al. (2009) and our model use a similar parametrization of the evolution the LF which can be compared. Both models found a very strong evolution in luminosity up to z=2 ($(1+z)^{3.4}$ for the Valiante et al. (2009) model; $(1+z)^{2.9\pm0.1}$ from z=0 to 0.87±0.05 and $(1+z)^{4.7\pm0.3}$ from z= 0.87±0.05 to 2 for our model). At larger redshift, our model is compatible with no evolution and the Valiante et al. (2009) model predicts a slight decrease in $(1+z)^{-1}$. Concerning the evolution in density, both models predicts an increase from z=0 to z≈1 (in $(1+z)^2$ for the Valiante et al. (2009) model and in $(1+z)^{0.8\pm0.2}$ for our model) and a decrease at larger redshift ($(1+z)^{-1.5}$ for the Valiante et al. (2009) model, $(1+z)^{-6.2\pm0.5}$ between z=0.87±0.5 and z=2 and $(1+z)^{-0.9\pm0.7}$ at z>2 for our model). These two models thus agree on the global shape of the evolution of the LF, but disagree on the values of the coefficient driving it. There is especially a large difference on the evolution density between z~ and z~2. This difference could be explained by different positions of the breaks. Nevertheless, the uncertainties on the Valiante et al. (2009) model are not estimated. It is thus hard to conclude.

Valiante et al. (2009) and Franceschini et al. (2010) used AGNs to reproduce the infrared observations. Valiante et al. (2009) also used a temperature dispersion of the galaxies. Our model reproduce the same observations using neither AGNs nor temperature dispersion. This show that the AGN contribution and the temperature scatter cannot be accurately constraint with this type of modeling.

8.2. Discriminating the models: smoking guns observations?

Although they use different galaxy populations and evolutions, the backwards evolution models reproduce the number counts from the mid-IR to the mm domain in a reasonably good way. It is thus important to find new observables to discriminate between models.

The comparison with the sub-mm redshift distributions of the bright sources is a rather simple, but very discriminant observations. For instance, the Fig. 7 shows significant difference of the sub-mm redshift distributions predicted by the different models. The Chapin et al. (2010) measurements performed on one small field with a cut at high flux is not sufficient to conclude. *Herschel* will help to increase the accuracy of the measured redshift distributions and to estimate the cosmic variance on them. These constraints will be crucial for the next generation of models.

Jauzac et al. (2010) showed that the redshift distribution of the contribution of the 24 microns sources to CIB at 70 and 160 μm ($d(\nu B_\nu)/dz$) is also a very discriminant constraint. The Fig. 18 shows the $d(\nu B_\nu)/dz$ at 350 μm. The different models make totally incompatible predictions in the sub-mm. An accurate measurement of $d(\nu B_\nu)/dz$ will be thus crucial for the future models.

8.3. Limits of our model

Our model is a useful tool to make a first interpretation of the observations from the mid-infrared to the mm domain. Nevertheless it is biased by some structural choice in its construction.

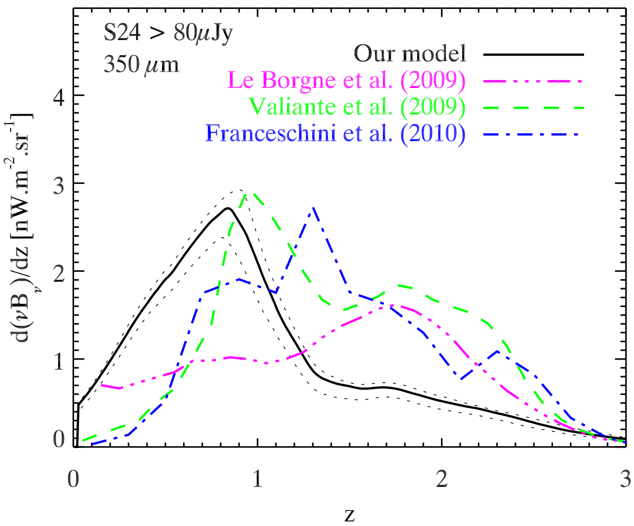

Figure 18. Differential contribution of the $S_{24} > 80\ \mu$Jy sources to the CIB as a function of the redshift at 350 μm. *Black solid line*: Our model (1-σ limit in *black dotted line*). *Purple three dot-dashed line*: Le Borgne et al. (2009) model. *Green dashed line*: Valiante et al. (2009) model. *Blue dot-dashed line*: Franceschini et al. (2010) model.

The choice of the parameters biases the results. For example, we have chosen the minimal number of parameters to reproduce the counts. If we would used more breaks in the evolution in density and in luminosity, the evolutions with the redshift would be smoother and the errors on the predictions would be different. Our errors are just the statistical errors due to the determination of the parameter of a given model using the data. It does not include the uncertainty on our hypothesis on the evolution (like α fixed) and the biases due to our choice of parameters (evolution in $(1+z)^r$ with breaks). For instance, the strong decrease in density between z~0.9 and z=2 is probably an artifact due to our choice of parametrization. In addition, our model of lensing is very simple and should be updated in the future. Nevertheless, the contribution of the lensing in the fitted data is low and the bias is thus negligible.

The backwards evolution models gives a very limited interpretation of the data. They are only a description of the evolution of the statistical properties of the infrared galaxies. The physical processes explaining the strong evolution of these objects are ignored. A more complex physical approach is thus necessary to deeply understand the history of the infrared galaxies. Nevertheless, our model is very useful to make a rapid interpretation of new observations and predictions for the future missions.

8.4. Perspectives

Our model fit the current data with rather simple hypotheses. Nevertheless, the increasing accuracy of the infrared observations will probably help us to refine it. Lots of updates will be possible when we will need a more complex model.

The α and σ parameters are fixed, but we can imagine an evolution of the shape of the LF with the redshift. A Fisher matrix analysis shows that the evolution of α at high redshift cannot be constraint without deeper observations in the sub-mm. An evolution of sigma could be constraints, but is not necessary to reproduce the current data.

The evolution of the parameters is very simple in the current version and could be updated in using more breaks or a smoother functional form.

The recent observations of *Herschel* will help a lot to update the SED used in our model, and maybe enable to determine their evolution with the redshift. The temperature of the big grain and its dispersion will be measured more accurately. Nevertheless, this dispersion must be modeled with a limited number of template to authorize MCMC approach. It is one of the future challenge for the evolution of our model.

Nevertheless, each refinement increases the number of free parameters of the model. It is important to limit the number of new parameters in comparison with the number of measurements.

9. Summary

- Our new parametric backwards evolution model reproduces the number counts from 15 μm to 1.1 mm, the monochromatic LF and the redshift distributions.
- Our model predicts a strong evolution in luminosity of the LF up to z=2 and a strong decrease in density from z=1 to z=2. We predict that the number of HyLIRG is maximum around z=2.
- We find that Normal galaxies, LIRG and ULIRG dominates the infrared output at z=0, z=1 and z=2, respectively. The HyLIRG accounts for a small fraction (<10%) at all redshifts.
- We reproduce the CIB spectrum and predict contributions per redshift and luminosity slice. We found that the mid- and far-infrared part of the CIB are mainly emitted by the normal galaxies and LIRG. The sub-mm part is mainly due to LIRG and ULIRG at high redshift in accordance with the sub-mm observations of deep fields. We estimated CIB total value of 23.7 ± 0.9 nW.m^{-2}.sr^{-1}.
- We estimate the fraction of lensed sources in the sub-mm as a function of the flux and wavelength. This contribution is low (< 10%) below 500 μm, but high (up to 50%) around 100 mJy in the mm domain.
- We predict that the population of very bright dusty galaxies detected by SPT and without IRAS counterpart (Vieira et al. 2009) is essentially composed of lensed sub-mm galaxies. We also predicts the contribution of the lensed sources to the *Planck* number counts.
- We predict the confusion limits for future missions like SPICA or CCAT.
- We estimate the opacity of the Universe to TeV photons.
- Material of the model (software, tables and predictions) is available at http://www.ias.u-psud.fr/irgalaxies/.

10. Conclusion

We showed that it is possible to reproduce the number counts from the mid-IR to the mm domain with a rather simple parametric model minimized automatically. Nevertheless, other automatically-tuned models reproduce the counts with different redshift distributions (Le Borgne et al. 2009; Marsden et al.

2010). It suggests that number counts only are not enough to build these models. Different observables are thus crucial to discriminate the different parametrization proposed by the model builders. These constraints are the luminosity functions, the redshift distributions, the P(D) or the fluctuations. These future measurements and their uncertainties have to be very robust to be directly fit by the next generation of models.

Acknowledgements. We acknowledge Mattia Negrello for explaining us how includes the lensing in our galaxy evolution model, Guillaume Patanchon for pushing us to make a parametric model, Nicolas Taburet and Marian Douspis for their explanations about the MCMC, Julien Grain for his explanations on the photon-photon interaction, Josh Younger for giving us useful references, Axel Weiβ and Alexandre Beelen for their discussion about the counts in the submm, and Morgane Cousin for carefully reading the draft and founding some mistakes. We also thank the BLAST team for the public release of their maps. We finally acknowledge Stefano Berta, Seb Oliver, Dave Clements, Axel Weiβ, Rosalind Hopwood, Joaquin Vieira, Andrew Hopkins, Alexandre Beelen and Kirsten Knudsen and Vandana Desai for providing us quickly their results. We also thanks Gaelen Marsden for our discussion about the comparison of our two models after the submission of our papers. This work was partially supported by the ANR-09-BLAN-0224-02.

References

Aharonian, F., Akhperjanian, A., Beilicke, M., et al. 2002, A&A, 393, 89
Aharonian, F., Akhperjanian, A., Beilicke, M., et al. 2003, A&A, 406, L9
Aharonian, F. A., Akhperjanian, A. G., Andronache, M., et al. 1999, A&A, 350, 757
Alexander, D. M., Bauer, F. E., Chapman, S. C., et al. 2005, ApJ, 632, 736
Austermann, J. E., Dunlop, J. S., Perera, T. A., et al. 2010, MNRAS, 401, 160
Baugh, C. M. 2006, Reports on Progress in Physics, 69, 3101
Bavouzet, N. 2008, PhD thesis, Université Paris-Sud 11
Beelen, A., Omont, A., Bavouzet, N., et al. 2008, A&A, 485, 645
Berta, S., Magnelli, B., Lutz, D., et al. 2010, ArXiv e-prints
Bertin, E., Dennefeld, M., & Moshir, M. 1997, A&A, 323, 685
Béthermin, M., Dole, H., Beelen, A., & Aussel, H. 2010a, A&A, 512, A78+
Béthermin, M., Dole, H., Cousin, M., & Bavouzet, N. 2010b, A&A, 516, A43+
Borys, C., Chapman, S., Halpern, M., & Scott, D. 2003, MNRAS, 344, 385
Caputi, K. I., Lagache, G., Yan, L., et al. 2007, ApJ, 660, 97
Chapin, E. L., Chapman, S. C., Coppin, K. E., et al. 2010, ArXiv e-prints
Chapin, E. L., Pope, A., Scott, D., et al. 2009, MNRAS, 398, 1793
Chapman, S. C., Blain, A. W., Smail, I., & Ivison, R. J. 2005, ApJ, 622, 772
Chib, S. & Greenberg, E. 1995, The American Statistician, 49, 325
Clements, D. L., Rigby, E., Maddox, S., et al. 2010, ArXiv e-prints
Cole, S., Lacey, C. G., Baugh, C. M., & Frenk, C. S. 2000, MNRAS, 319, 168
Condon, J. J. 1974, ApJ, 188, 279
Coppin, K., Chapin, E. L., Mortier, A. M. J., et al. 2006, MNRAS, 372, 1621
Desai, V., Soifer, B. T., Dey, A., et al. 2008, ApJ, 679, 1204
Devlin, M. J., Ade, P. A. R., Aretxaga, I., et al. 2009, Nature, 458, 737
Dole, H., Lagache, G., & Puget, J. 2003, ApJ, 585, 617
Dole, H., Lagache, G., Puget, J., et al. 2006, A&A, 451, 417
Dominguez, A., Primack, J. R., Rosario, D. J., et al. 2010, ArXiv e-prints
Driver, S. P., Popescu, C. C., Tuffs, R. J., et al. 2008, ApJ, 678, L101
Dunkley, J., Bucher, M., Ferreira, P. G., Moodley, K., & Skordis, C. 2005, MNRAS, 356, 925
Dwek, E. & Krennrich, F. 2005, ApJ, 618, 657
Elbaz, D., Cesarsky, C. J., Fadda, D., et al. 1999, A&A, 351, L37
Engelbracht, C. W., Blaylock, M., Su, K. Y. L., et al. 2007, PASP, 119, 994
Fadda, D., Yan, L., Lagache, G., et al. 2010, ArXiv e-prints
Fernandez-Conde, N., Lagache, G., Puget, J., & Dole, H. 2008, A&A, 481, 885
Fernandez-Conde, N., Lagache, G., Puget, J., & Dole, H. 2010, A&A, 515, A48+
Fixsen, D. J. 2009, ApJ, 707, 916
Franceschini, A., Rodighiero, G., Vaccari, M., et al. 2010, A&A, 517, A74+
Frayer, D. T., Sanders, D. B., Surace, J. A., et al. 2009, AJ, 138, 1261
Glenn, J., Conley, A., Béthermin, M., & Consorsium, H. 2010, in prep.
Gordon, K. D., Engelbracht, C. W., Fadda, D., et al. 2007, PASP, 119, 1019
Gregorich, D. T., Neugebauer, G., Soifer, B. T., Gunn, J. E., & Herter, T. L. 1995, AJ, 110, 259
Greve, T. R., Weiss, A., Walter, F., et al. 2009, ArXiv e-prints
Griffin, M. e. a. 2010, in prep.
Gruppioni, C., Lari, C., Pozzi, F., et al. 2002, MNRAS, 335, 831
Hacking, P. & Houck, J. R. 1987, ApJS, 63, 311
Hall, N. R., Keisler, R., Knox, L., et al. 2010, ApJ, 718, 632
Heitler, W. 1954, Quantum theory of radiation, ed. Heitler, W.
Hezaveh, Y. D. & Holder, G. P. 2010, ArXiv e-prints
Hogg, D. W. 1999, ArXiv Astrophysics e-prints
Hopkins, A. M. & Beacom, J. F. 2006, ApJ, 651, 142
Hopwood, R., Serjeant, S., Negrello, M., et al. 2010, ArXiv e-prints
Imanishi, M. 2009, ApJ, 694, 751
Ishihara, D., Onaka, T., Kataza, H., et al. 2010, A&A, 514, A1+
Jauch, J. M. & Rohrlich, F. 1976, The theory of photons and electrons. The relativistic quantum field theory of charged particles with spin one-half, ed. Jauch, J. M. & Rohrlich, F.
Jauzac, M., Dole, H., Le Floc'h, E., et al. 2010, A&A, sub.
Kennicutt, Jr., R. C. 1998, ApJ, 498, 541
Knudsen, K. K., van der Werf, P. P., & Kneib, J. 2008, MNRAS, 384, 1611
Lacey, C. G., Baugh, C. M., Frenk, C. S., et al. 2010, MNRAS, 443
Lagache, G., Abergel, A., Boulanger, F., Désert, F. X., & Puget, J. 1999, A&A, 344, 322
Lagache, G., Bavouzet, N., Fernandez-Conde, N., et al. 2007, ApJ, 665, L89
Lagache, G., Dole, H., Puget, J.-L., et al. 2004, ApJS, 154, 112
Lagache, G., Haffner, L. M., Reynolds, R. J., & Tufte, S. L. 2000, A&A, 354, 247
Lagache, G., Puget, J., & Dole, H. 2005, ARA&A, 43, 727
Lanzoni, B., Guiderdoni, B., Mamon, G. A., Devriendt, J., & Hatton, S. 2005, MNRAS, 361, 369
Larson, D., Dunkley, J., Hinshaw, G., et al. 2010, ArXiv e-prints
Le Borgne, D., Elbaz, D., Ocvirk, P., & Pichon, C. 2009, A&A, 504, 727
Le Floc'h, E., Aussel, H., Ilbert, O., et al. 2009, ApJ, 703, 222
Le Floc'h, E., Papovich, C., Dole, H., et al. 2005, ApJ, 632, 169
Lima, M., Jain, B., Devlin, M., & Aguirre, J. 2010, ApJ, 717, L31
Lonsdale, C. J., Hacking, P. B., Conrow, T. P., & Rowan-Robinson, M. 1990, ApJ, 358, 60
Magnelli, B., Elbaz, D., Chary, R. R., et al. 2009, A&A, 496, 57
Marsden, G., Ade, P. A. R., Bock, J. J., et al. 2009, ApJ, 707, 1729
Marsden, G., Chapin, E. L., Halpern, M., et al. 2010, ArXiv e-prints
Matsuura, S., Shirahata, M., Kawada, M., et al. 2010, ArXiv e-prints
Miville-Deschênes, M., Lagache, G., & Puget, J. 2002, A&A, 393, 749
Negrello, M., Hopwood, R., De Zotti, G., et al. 2010, Science, 330, 800
Negrello, M., Perrotta, F., González-Nuevo, J., et al. 2007, MNRAS, 377, 1557
Nguyen, H. T., Schulz, B., Levenson, L., et al. 2010, ArXiv e-prints
Oliver, S. J., Wang, L., Smith, A. J., et al. 2010, ArXiv e-prints
Papovich, C., Dole, H., Egami, E., et al. 2004, ApJS, 154, 70
Pascale, E., Ade, P. A. R., Bock, J. J., et al. 2008, ApJ, 681, 400
Pascale, E., Ade, P. A. R., Bock, J. J., et al. 2009, ApJ, 707, 1740
Patanchon, G., Ade, P. A. R., Bock, J. J., et al. 2009, ApJ, 707, 1750
Pearson, C. P., Oyabu, S., Wada, T., et al. 2010, A&A, 514, A8+
Penin, A., Doré, O., Lagache, G., & Béthermin, M. 2010, in prep.
Perrotta, F., Baccigalupi, C., Bartelmann, M., De Zotti, G., & Granato, G. L. 2002, MNRAS, 329, 445
Perrotta, F., Magliocchetti, M., Baccigalupi, C., et al. 2001, ArXiv Astrophysics e-prints
Pilbratt, G. & al. 2010, in prep.
Puget, J., Abergel, A., Bernard, J., et al. 1996, A&A, 308, L5+
Reddy, N. A., Steidel, C. C., Pettini, M., et al. 2008, ApJS, 175, 48
Reed, D. S., Bower, R., Frenk, C. S., Jenkins, A., & Theuns, T. 2007, MNRAS, 374, 2
Renault, C., Barrau, A., Lagache, G., & Puget, J. 2001, A&A, 371, 771
Rodighiero, G., Vaccari, M., Franceschini, A., et al. 2009, ArXiv e-prints
Rowan-Robinson, M. 2009, MNRAS, 394, 117
Rowan-Robinson, M., Hughes, J., Vedi, K., & Walker, D. W. 1990, MNRAS, 246, 273
Saunders, W., Rowan-Robinson, M., Lawrence, A., et al. 1990, MNRAS, 242, 318
Scott, K. S., Yun, M. S., Wilson, G. W., et al. 2010, MNRAS, 684
Scott, S. E., Dunlop, J. S., & Serjeant, S. 2006, MNRAS, 370, 1057
Shupe, D. L., Rowan-Robinson, M., Lonsdale, C. J., et al. 2008, AJ, 135, 1050
Smail, I., Ivison, R. J., Blain, A. W., & Kneib, J. 2002, MNRAS, 331, 495
Soifer, B. T. & Neugebauer, G. 1991, AJ, 101, 354
Stansberry, J. A., Gordon, K. D., Bhattacharya, B., et al. 2007, PASP, 119, 1038
Stecker, F. W. & de Jager, O. C. 1997, ApJ, 476, 712
Swinyard, B. M., Ade, P., Baluteau, J., et al. 2010, A&A, 518, L4+
Takeuchi, T. T. & Ishii, T. T. 2004, ApJ, 604, 40
Teplitz, H. I., Chary, R., Elbaz, D., et al. 2010, ArXiv e-prints
Truch, M. D. P., Ade, P. A. R., Bock, J. J., et al. 2009, ApJ, 707, 1723
Vaccari, M., Marchetti, L., Franceschini, A., et al. 2010, ArXiv e-prints
Valiante, E., Lutz, D., Sturm, E., Genzel, R., & Chapin, E. L. 2009, ApJ, 701, 1814
Vieira, J. D., Crawford, T. M., Switzer, E. R., et al. 2009, ArXiv e-prints
Viero, M. P., Ade, P. A. R., Bock, J. J., et al. 2009, ApJ, 707, 1766
Weiß, A., Kovács, A., Coppin, K., et al. 2009, ApJ, 707, 1201
Wilman, R. J., Jarvis, M. J., Mauch, T., Rawlings, S., & Hickey, S. 2010, MNRAS, 406

λ μm	$5\sigma_{conf,P(D)}$ mJy	CIB fraction[a] %	$S_{conf,density}$ mJy	CIB fraction[b] %
24	5.62×10^{-2}	83.1	7.51×10^{-2}	72.3
70	3.09×10^{0}	51.5	2.88×10^{0}	48.8
100	1.38×10^{1}	36.3	1.15×10^{1}	36.1
160	5.84×10^{1}	12.3	3.43×10^{1}	17.2
250	1.06×10^{2}	3.2	4.41×10^{1}	6.9
350	1.13×10^{2}	0.8	3.57×10^{1}	3.0
500	9.18×10^{1}	0.2	2.24×10^{1}	1.4
850	4.12×10^{1}	100.0	9.25×10^{0}	0.7
1100	2.76×10^{1}	100.0	6.25×10^{0}	0.5

Notes. [a] Fraction of the CIB resolved at 5-σ_{conf}.
[b] Fraction of the CIB resolved at the flux limit.

Table 6. Confusion noise and resolved fraction of the CIB at different wavelengths for a 0.85 m telescope(*Spitzer* like).

λ μm	$5\sigma_{conf,P(D)}$ mJy	CIB fraction[a] %	$S_{conf,density}$ mJy	CIB fraction[b] %
70	7.95×10^{-2}	96.4	1.20×10^{-1}	91.8
100	5.13×10^{-1}	90.8	7.75×10^{-1}	83.9
160	5.01×10^{0}	67.8	5.93×10^{0}	59.8
250	1.75×10^{1}	25.9	1.28×10^{1}	29.6
350	2.30×10^{1}	9.2	1.28×10^{1}	15.8
500	2.08×10^{1}	3.3	9.24×10^{0}	8.7
850	1.13×10^{1}	1.5	3.88×10^{0}	4.4
1100	8.40×10^{0}	1.2	2.66×10^{0}	3.5

Notes. [a] Fraction of the CIB resolved at 5-σ_{conf}.
[b] Fraction of the CIB resolved at the flux limit.

Table 7. Confusion noise and resolved fraction of the CIB at different wavelengths for a 3.29 m telescope (*Herschel* like).

λ μm	$5\sigma_{conf,P(D)}$ mJy	CIB fraction[a] %	$S_{conf,density}$ mJy	CIB fraction[b] %
160	5.86×10^{-2}	99.4	5.55×10^{-2}	98.2
250	7.06×10^{-1}	94.2	1.11×10^{0}	85.6
350	2.08×10^{0}	77.9	2.57×10^{0}	63.2
500	3.05×10^{0}	50.0	2.57×10^{0}	41.8
850	2.19×10^{0}	23.6	1.24×10^{0}	22.9
1100	1.74×10^{0}	18.4	8.74×10^{-1}	18.6

Notes. [a] Fraction of the CIB resolved at 5-σ_{conf}.
[b] Fraction of the CIB resolved at the flux limit.

Table 8. Confusion noise and resolved fraction of the CIB at different wavelengths for a 12.00 m telescope (APEX like).

Younger, J. D. & Hopkins, P. F. 2010, ArXiv e-prints
Zemcov, M., Blain, A., Halpern, M., & Levenson, L. 2010, ApJ, 721, 424

λ μm	$5\sigma_{conf,P(D)}$ mJy	CIB fraction[a] %	$S_{conf,density}$ mJy	CIB fraction[b] %
160	2.34×10^{-2}	99.8	1.04×10^{-2}	99.3
250	3.01×10^{-1}	97.6	4.48×10^{-1}	92.5
350	1.08×10^{0}	88.6	1.55×10^{0}	74.7
500	1.87×10^{0}	66.6	1.86×10^{0}	52.4
850	1.55×10^{0}	33.8	9.70×10^{-1}	29.4
1100	1.26×10^{0}	26.7	6.89×10^{-1}	24.1

Notes. [a] Fraction of the CIB resolved at 5-σ_{conf}.
[b] Fraction of the CIB resolved at the flux limit.

Table 9. Confusion noise and resolved fraction of the CIB at different wavelengths for a 15.00 m telescope (CSO like).

λ μm	$5\sigma_{conf,P(D)}$ mJy	CIB fraction[a] %	$S_{conf,density}$ mJy	CIB fraction[b] %
250	2.81×10^{-2}	99.8	1.32×10^{-2}	99.1
350	1.57×10^{-1}	98.5	2.12×10^{-1}	94.2
500	4.31×10^{-1}	92.6	6.09×10^{-1}	79.1
850	5.99×10^{-1}	64.6	4.62×10^{-1}	49.7
1100	5.39×10^{-1}	53.1	3.46×10^{-1}	41.2

Notes. [a] Fraction of the CIB resolved at 5-σ_{conf}.
[b] Fraction of the CIB resolved at the flux limit.

Table 10. Confusion noise and resolved fraction of the CIB at different wavelengths for a 25.00 m telescope (CCAT like).